Word Count: 10456

# Development of soft magnetic composites for magnetized pavement to improve the efficiency of electric vehicle's wireless power transfer

Yanjie Li[1], Feng Li[1], Siqi Zhou[1*], Xiaolei Ma[1], Yue Hou[2]

[1] Beijing Key Laboratory for Cooperative Vehicle Infrastructure Systems and Safety Control, School of Transportation Science and Engineering, Beihang University, Beijing 100191, China

[2] Department of Civil Engineering, Faculty of Science and Engineering, Swansea University, Swansea, SA2 8PP, UK

[*] Corresponding author. E-mail: zsq47@buaa.edu.cn, Tel: +8618601266994

## Abstract

Integrating the wireless power transfer (WPT) system into the pavement is an effective way to solve the inconvenience of electric vehicles (EVs)' charging, accelerating the growth of ownership of EVs to achieve net carbon zero in transportation. However, the existence of a cement paving layer between coils was a negative impact factor. Here, two types of ferrite powders were separately mixed into the cement to prepare soft magnetic composite (SMC) material to enhance the coupling degree of coils. The magnetic and mechanical performance of the composite were tested by a vibrating sample magnetometer and compressive and flexural strength tester. Furthermore, to explore the optimal layout of the magnetized pavement structure, nine pavement layouts were designed based on the distribution of magnetic flux. Finally, the effect of SMC material on improving the charging performance was verified by WPT system test platform. Results showed that the Ni-Zn ferrite powder exhibited superior magnetic permeability due to its stronger magnetic moments and lower magnetic domain wall energy compared to Mn-Zn ferrite powder. The peak relative permeability of SMC materials reached 14.370 with an equal mass ratio of Ni-Zn ferrite powder to cement. Conversely, optimal strength was attained with a Mn-Zn ferrite to cement ratio of 0.2, resulting in a compressive strength of 36 MPa and a flexural strength of 4.0 MPa. Strategically placing SMC within the pavement, both in the core's interior and exterior to the coil, enhanced the coupling coefficient of coils, thereby improving the transmission efficiency of the WPT system. The incorporation of Ni-Zn ferrite powder in a 1:1 mass ratio to cement materialized the highest efficiency. Nonetheless, considering the mechanical performance, the SMC material with a 0.6 mass ratio of Mn-Zn ferrite powder to cement was recommended for magnetized pavements. The WPT system test results showed a transmission efficiency of 89.78% when utilizing magnetized pavement, surpassing the efficiency with the whole pavement material by 1.36%, which

indicated great value and potential in energy conservation and carbon reduction of employing magnetized pavement in WPT technology.

**Keywords:** Magnetized pavement, Cement, Soft magnetic composites material, Wireless power transfer, Efficiency

## List of Nomenclature

*Abbreviation*

| Abbreviation | Full name |
|---|---|
| EVs | Electric vehicles |
| WPT | Wireless power transfer |
| V2X | Vehicle to everything |
| SMC | Soft magnetic composite |
| Mn-Zn | Manganese-zinc |
| Ni-Zn | Nickel-zinc |
| XRF | X-ray fluorescence |
| SEM | Scanning electron microscope |
| VSM | Vibrating sample magnetometer |
| SEM-EDS | Scanning electron microscope equipped with energy dispersive spectroscopy |
| SS | Series-series |
| C-S-H | Calcium silicate hydrate |

*Parameters*

| Parameters | Definition |
|---|---|
| $Z_1$ | Impedance of the primary side circuit [Ω] |
| $Z_2$ | Impedance of the secondary side circuit [Ω] |
| $I_1$ | Current in primary circuit [A] |
| $I_2$ | Current in secondary circuit [A] |
| $j$ | Imaginary unit |
| $\omega$ | Frequency of power supply [Hz] |
| $M_L$ | Mutual inductance [H] |
| $\omega$ | Frequency of power supply [Hz] |
| $\omega_0$ | Resonant frequency [Hz] |
| $L_1$ | Self-inductance of the primary coil [H] |
| $L_2$ | Self-inductance of the secondary coil [H] |
| $U_s$ | High-frequency power supply [V] |

| | |
|---|---|
| $C_1$ | Compensation capacitor of primary circuit [F] |
| $C_2$ | Compensation capacitor of secondary circuit [F] |
| $R_1$ | Equivalent resistance of primary coil [Ω] |
| $R_2$ | Equivalent resistance of secondary coil [Ω] |
| $R_L$ | Resistive load [Ω] |
| $k$ | Coupling coefficient |
| $P$ | Output power [W] |
| $\eta$ | Transmission efficiency |
| $R_{in}$ | Inner radius of the coil [Ω] |
| $R_{out}$ | Outer radius of the coil [Ω] |
| $MF$ | The region where the magnetic flux density outside the coil exceeded 0.0001 T |
| $\overrightarrow{\mu_l}$ | Electron orbital magnetic moments [A•$m^2$] |
| $\overrightarrow{\mu_s}$ | Electron spin magnetic moments [A•$m^2$] |
| $\overrightarrow{\mu_L}$ | Total orbital magnetic moment [A•$m^2$] |
| $\overrightarrow{\mu_S}$ | Total spin magnetic moment [A•$m^2$] |
| $\overrightarrow{\mu_M}$ | Electron magnetic moments [A•$m^2$] |
| $L$ | Total orbital angular momentum quantum number |
| $\gamma_s$ | Gyromagnetic ratio of the electron spin [m•$s^{-1}$•$A^{-1}$] |
| $S$ | Total spin quantum number |
| $g_J$ | Lande g-factor |
| $J$ | Total angular momentum quantum number of an atom |
| $M$ | Magnetization intensity [A•$m^{-1}$] |
| $\vec{B}$ | External magnetic field [T] |
| $\overrightarrow{B'}$ | Induced magnetic field [T] |
| $\overrightarrow{B'_{in}}$ | Induced magnetic field with the same direction as the external magnetic field [T] |
| $\overrightarrow{B'_{out}}$, | Induced magnetic field with the opposite direction as the external magnetic field [T] |
| $\overrightarrow{B_{L-1}}$ | The sum of $\vec{B}$ and $\overrightarrow{B'_{out}}$ [T] |
| $\overrightarrow{B_{L-2}}$ | The sum of $\vec{B}$ and $\overrightarrow{B'_{in}}$ [T] |
| $\overrightarrow{B_{H-1}}$ | The magnetic field in Example-region-1 [T] |
| $\overrightarrow{B_{H-2}}$ | The magnetic field in Example-region-2 [T] |
| $\overrightarrow{B''_{in}}$ | Induced magnetic field from another ferrite particle with the same direction as the external magnetic field [T] |
| $\overrightarrow{B''_{out}}$ | Induced magnetic field from another ferrite particle with the opposite direction as the external magnetic field [T] |
| $\Phi_L$ | Magnetic flux in two regions when the distance between magnetic particles is large [Wb] |

| | |
|---|---|
| $\Phi_H$ | Magnetic flux in two regions when the distance between magnetic particles is small [Wb] |
| $H_{eff}$ | Coercivity [Oe] |
| $\gamma$ | Magnetic domain wall energy [J•m$^{-2}$] |
| $J_S$ | Magnetic polarization strength [A•m$^{-1}$] |
| $d$ | Magnetic domain wall width [μm] |
| $N$ | Demagnetization factor |
| $D$ | Magnetic particle diameter [μm] |
| $\alpha$ | Parameter related to the domain shape |
| $S_V$ | Magnetic domain wall area per unit volume [μm$^{-1}$] |
| $\mu_r$ | Relative permeability |
| $\mu_0$ | Permeability of vacuum [H•m$^{-1}$] |
| $N_L$ | Number of coil turns |
| $r$ | Radius of coils [mm] |
| $a$ | Winding radius [mm] |
| $N_1$ | Number of primary coil turns |
| $N_2$ | Number of secondary coil turns |
| $T$ | Transmission distance between coils [mm] |
| $r_1$ | Radius of the primary coil [mm] |
| $r_2$ | Radius of the secondary coil [mm] |

## 1 Introduction

Electric vehicles (EVs) are considered an attractive alternative to traditional internal combustion engine vehicle since it has higher energy efficiency and lower exhaust emission (Bi et al., 2021; Crabtree, 2019; Lal and You, 2023). The shortcomings of EVs such as short driving range, limited battery capacity, unreasonable distribution of charging piles, and long charging time have always been important bottlenecks restricting the development of EVs (Hu et al., 2020). Wireless Power Transfer (WPT) technology integrated into the road can realize the charging of EVs while driving, which is expected to become an important supplement to wired charging and solve the shortcomings of EVs (Limb et al., 2018; Rubino et al., 2017; Thomas, 2023). The application of WPT will also help promote the development of intelligent transportation infrastructure, as it can be combined with Vehicle to Everything (V2X) technology to power sensors embedded in the pavement (Bi et al., 2022; Shang et al., 2022; Shang et al., 2021).

The coupling mechanism composed of a primary coil and a secondary coil is the core of the WPT system, determining the charging performance. In practical application, to ensure safety and durability, the primary coil needs to be embedded inside the pavement structure, causing part of the transmission medium to be replaced by the pavement material from the air (Ceravolo et al., 2017; Ceravolo et al., 2016; Chen and Kringos, 2014). The existence of a pavement layer between coils negatively impacts both the coupling degree and self-inductance of the coils, as identified by most previous studies (Li et al., 2021; Onar et al., 2013). It has been reported that when using 5 cm thick AC-13 pavement material, both the self-inductance of the primary side coil and the coupling coefficient between the coils changed by 1.5% (Li et al., 2021). Onar et al. (2013) used a 110 mm thick pavement cement concrete sample as the transmission media and found that the energy loss had nearly doubled. This is because the pavement material obstructs the propagation of the magnetic field to the secondary coil, resulting in the decrease of the coupling degree of the coils and further reducing the efficiency of the WPT system (Guo and Wang, 2022; Li et al., 2021). Pavement material is a mixture of binder and aggregate that contains numerous pores. As electromagnetic waves propagate through the pavement material, they undergo reflection, transmission, and refraction at multiple interfaces, leading to changes in the electromagnetic wave transmission direction and an increase in energy loss (Edwards et al., 2019; Lu et al., 2024b). It is specified in GB/T38775.3 (2020) that the transmission efficiency of the WPT system should not be less than 85%.

To guide the direction of magnetic field propagation between coils, reduce energy loss, and ensure that the transmission efficiency meets the requirements of the specification, a promising solution is to incorporate magnetic materials into the surface layer of pavement above the primary coil. Soft magnetic composite (SMC) materials, widely used in electronics and metallurgy applications, offer advantages such as high permeability and low coercivity, making them effective at gathering dissipated magnetic flux (Birčáková et al., 2022; Gu et al., 2022b). They can also generate induced magnetic fields to enhance the original magnetic field (Tavakoli et al., 2017; Trompetter et al., 2023). SMC materials are typically prepared by mixing magnetic powder particles into a non-magnetic polymer or alloy medium, and pressed under high temperature and pressure (Kim et al., 2018; Thorsson et al., 2022; Wang et al., 2021). The sample size that can be prepared in this way is very small. To be applied in pavement engineering, the research on the preparation of SMC has gradually attracted attention. This involves mixing iron powder (Gu et al., 2023), magnetite (Mahmud et al., 2017), stainless-steel fibers (Edwards et al., 2019), and other magnetic materials with binding material such as cement (Gu et al., 2022a; Lu et al., 2023b; Meng et al., 2024), geopolymer (Gu et al., 2023; Gu et al., 2022b; Li et al., 2024) and asphalt (Liu et al., 2020b; Zhang et al., 2023) to form the matrix. In the technology of melting ice by induction heating, a layer of SMC material is placed underneath the induction heating coils to serving as a generation layer. This reduces the amount of dissipated electromagnetic energy and validates the effectiveness of the SMC materials in guiding the magnetic field (Liu et al., 2020a; Liu et al., 2019). Additionally, magnetic materials, especially ferrite particles, are also used to develop self-healing asphalt concrete due to their excellent magnetic properties (Lu et al., 2024a; Lu et al., 2023a). In wireless charging technology, the use of SMC material as both magnetic shielding plates and magnetic cores for the primary coils has been shown to reduce magnetic field leakage and guide the magnetic fields along the core direction, thereby improving charging efficiency (Tavakoli et al., 2017). However, the effect of introducing SMC materials into the pavement surface layer to guide the propagation of the magnetic field and improve the coupling degree of the primary and secondary coils is still to be explored. Therefore, this work aims to develop a kind of SMC material for wireless charging pavement and verify its effectiveness in improving the performance of the WPT system.

On the other hand, determining the optimal placement of SMC material within the pavement surface layer is also worth considering. In WPT technology, a high-permeability ferrite plate is usually placed on the back of the coils to reduce magnetic field leakage (Kim et al., 2016; Pei et al., 2021). The underlying principle is that the high-permeability magnetic material creates paths of low magnetic resistance, and the magnetic field lines tend to propagate in the direction of low magnetic resistance. Therefore, the magnetic field lines enter the ferrite plate and travel along the side length direction of the ferrite plate until they exit the interface (Talluri et al., 2021). After adopting this shielding measure, there are almost no magnetic field lines perpendicular to the plane of the coil on the back of the ferrite. By comparison, if the SMC materials developed in this study are used to replace all the pavement materials and placed on the upper layer of the primary coil as a whole directly, it will have a shielding effect on the magnetic field between the primary and secondary sides rather than an enhancing effect. This hypothesis was also verified in the preliminary experiment. To utilize the magnetic field guidance function of SMC materials, that is, to transmit the magnetic field along the magnetic material to the secondary coil, designing the layout of SMC within the pavement layer based on the magnetic flux distribution between the coils remains a challenging problem.

In this work, cement served as the matrix, with two types of ferrite powders, manganese-zinc (Mn-Zn) ferrite powder, and nickel-zinc (Ni-Zn) ferrite powder - selected to prepare SMC material with varying contents. The differences in magnetic permeability were analyzed, and the mechanical properties of the SMC material were also explored. The pavement surface was divided into seven regions based on the distribution of magnetic flux paths between the primary and secondary coils, and nine layouts were designed using different materials for each region. A simulation model of the WPT system including magnetized pavement and coupling coils was established. This model explored the influence of introducing SMC material into the pavement on the resonance induction coupling process which successfully demonstrated the energy-saving potential by magnetized road surface for WPT system.

## 2 Materials and methods

### 2.1 Raw materials

To prepare SMC specimens, cement powder (P.S.A 32.5R grade) and two types of ferrite powder, Mn-Zn and Ni-Zn, were mixed with water. Cement was sourced from Yanxin Holding Group Co., Ltd., China, and the ferrite powder from Suzhou Yibensai Electronic Technology Co., Ltd., China. The ferrite powder was sintered during the manufacturing process. The main chemical composition and the particle size distribution of the raw materials were determined by X-ray fluorescence spectroscopy (XRF, ARL Advant X Intellipower TM3600) and a Malvern Mastersizer 2000 Laser Particle Analyzer, respectively. Microstructural images of the ferrite powders were obtained using the Scanning Electron Microscope (SEM) test model Hitachi SU8020.

### 2.2 Mix design

Cement, ferrite powders, and water were mixed and stirred to prepare the SMC material. Before the preparation of SMC and cement paste, some exploratory experiments were carried out to make the paste fluidity suitable. The results showed that the water-solid ratio of specimens should be fixed at a ratio of 0.33 during sample preparation. Then, seven cement pastes were prepared by varying the type of ferrite powder and the proportion of ferrite and cement. Details of the mix design are shown in Table 1. After preparation, the fresh pastes were poured into iron molds with a length of 160 mm, a width of 40 mm, and a height of 40 mm, and cured for 24 hours in a standard curing box (Temperature: 20 ± 2 ◦C; Humidity: 95 ± 2%) to harden. The hardened samples were demolded and subsequently cured under standard conditions for 7d and 28 days, respectively.

**Table 1** Mix design of SMC materials.

| Specimen No. | Cement powder(g) | Ferrite/Cement | Ferrite powder(g) | Water/Solid | Water(g) |
|---|---|---|---|---|---|
| Ce | 1500 | 0 | 0 | 0.33 | 495 |
| M/C-02 | 1250 | 0.2 | 250 | 0.33 | 495 |
| M/C-06 | 937.5 | 0.6 | 562.5 | 0.33 | 495 |
| M/C-10 | 750 | 1 | 750 | 0.33 | 495 |
| N/C-02 | 1250 | 0.2 | 250 | 0.33 | 495 |
| N/C-06 | 937.5 | 0.6 | 562.5 | 0.33 | 495 |
| N/C-10 | 750 | 1 | 750 | 0.33 | 495 |

### 2.3 Material testing and characterization methods

The vibrating sample magnetometer (VSM, Lake Shore 7407) was adopted to test the magnetic hysteresis loops of ferrite powders and SMC material after 28d curing according to Chinese standard GB/T 3848-2017 (2017). The instrument has a sensitivity of $5 \times 10^{-7}$ emu and an accuracy of 2%. During the test, the maximum applied magnetic field was set to 3 T. In terms of mechanical properties, the flexural strength and compressive strength of hardening SMC samples were tested according to the specification of GB/T 17671-2021 (2021) after they had been cured for 7 days. TYE-3000 compressive testing machine produced by Wuxi Jianyi Instrument Machinery Co., LTD. was adopted. During one test run, a flexural strength test was conducted on three specimens of size 40 mm * 40 mm * 160 mm with a controlled loading rate of 50 N/s ± 10 N/s. The specimens that broke into two pieces during the test were then utilized for subsequent compressive strength tests, resulting in a total of six specimens tested for compressive strength in the same run. The loading rate for the compressive strength tests was controlled at 2400 N/s ± 200 N/s. A Hitachi SU8020 scanning electron microscope equipped with energy dispersive spectroscopy (SEM-EDS) was employed to observe the microscopic morphology and elemental components of SMC materials. After undergoing compressive and flexural strength tests, the fractured specimens were carefully broken down until at least three block-shaped samples were obtained for SEM-EDS analysis, each with dimensions smaller than 1 cm in length, width, and height. During the examination, manganese was selected as the marker element for energy spectrum scanning, with an acceleration voltage set at 20.0 kV and a magnification of 3000x.

## 3 WPT system for series – series topology

### 3.1 Theoretical analysis of the WPT system

The principle of the WPT system is based on Faraday's law of electromagnetic induction. The high-frequency power supply provides alternating current for the primary circuit, generating a changing magnetic field in the primary side coil. After traveling through the air, the changing magnetic field is captured by the secondary coil, which generates an induced electromotive force, thereby charging the EVs and completing the energy transmission process (Liu et al., 2017). Fig. 1 shows the most basic compensation topology used in WPT systems, i.e., the Series-Series (SS) topology consisting of a single capacitor and inductor in series (Rasekh et al., 2020; Yang et al., 2018). According to the mutual inductance theory and Kirchhoff's Voltage Laws, the physical relationship in Fig. 1 is shown in Eqs. (1)-(3).

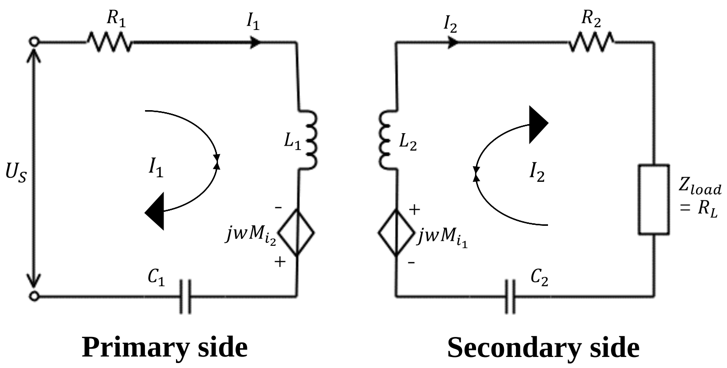


**Fig. 1.** Series-Series topologies for primary and secondary resonant circuits.

$$\begin{cases} Z_1 I_1 - j\omega M_L I_2 = U_s \\ Z_2 I_2 - j\omega M_L I_1 = 0 \end{cases} \tag{1}$$

$$Z_1(j\omega) = -j\frac{1}{\omega C_1} + j\omega L_1 + R_1 \tag{2}$$

$$Z_2(j\omega) = -j\frac{1}{\omega C_2} + j\omega L_2 + R_2 + R_L \tag{3}$$

where $U_s$ is the voltage of high-frequency supply, $\omega$ is the angular frequency of $U_s$, and $j$ is the imaginary unit. The compensation capacitors are $C_1$ and $C_2$. And $R_L$ is the charging load on the secondary side. $R_1$ and $R_2$ are the equivalent resistances of circuits. $I_1$ and $I_2$ are current in primary and secondary circuits, respectively. $L_1$ and $L_2$ are self-inductances of the coils, with $M_L$ as mutual inductance. The mutual coupling effect is described by coupling coefficient $k$. The calculation formula of $k$ is shown in Eq. (4).

$$k = {M_L}/{\sqrt{L_1 L_2}} \tag{4}$$

When the SS topological resonant circuit is in the resonant state, the capacitive reactance can offset the inductive reactance of the inductor, making the circuit present pure resistance, namely $Z_1 = R_1$, $Z_2 = R_2 + R_L$. To maximize the transmission efficiency of the WPT system, the resonant frequencies of the primary circuit and the secondary circuit should be the same. This ensures that both circuits reach the resonant state simultaneously. The calculation formula of resonant frequency is shown in Eq. (5).

$$\omega_0 = \frac{1}{\sqrt{L_1 C_1}} = \frac{1}{\sqrt{L_2 C_2}} \tag{5}$$

The current of the primary coil and the secondary side coil can be obtained as Eq. (6) and Eq. (7):

$$I_1 = \frac{U_S}{R_1 + \frac{{\omega_0}^2 {M_L}^2}{R_2 + R_L}} \tag{6}$$

$$I_2 = \frac{j\omega M_L I_1}{(R_2 + R_L)} \tag{7}$$

Finally, the output power and transmission efficiency of the system can be calculated through Eqs. (8)-(9). The values used for some parameters are shown in Table 2. According to Eqs. (6)-(8), the current in the primary and secondary circuits is directly proportional to the value of *Us*. To ensure safety, it is crucial to limit the current and output power. This paper targeted an output power of 280 W, as referenced in (Li et al., 2021), with the supply voltage determined to be 85 V determined through preliminary experiments. In accordance with regulatory standards, the frequency of WPT systems should be between 79-90 kHz, with 85 kHz being the most commonly used frequency (Chen et al., 2023; Standard, 2023; Zhang et al., 2024). Building on prior work, this study continued to utilize a resonant frequency of approximately 85.5 kHz for the WPT system (Li et al., 2022). The value of $R_L$ influences the system's operational characteristics. By differentiating the formula of transmission efficiency with respect to $R_L$, the value of $R_L$ corresponding to peak efficiency can be determined. Calculations within this study suggested that $R_L$ should be set to 25 Ω. This study maintained the structural parameters of the primary and secondary coils as delineated in (Li et al., 2021), setting $R_1$ and $R_2$ at 1 Ω following their findings.

$$P = \frac{{\omega_0}^2 k^2 L_1 L_2 {U_S}^2 R_L}{(R_1(R_2 + R_L) + {\omega_0}^2 k^2 L_1 L_2)^2} \tag{8}$$

$$\eta = \frac{R_L}{R_2 + R_L} \times \frac{{\omega_0}^2 k^2 L_1 L_2}{R_1(R_2 + R_L) + {\omega_0}^2 k^2 L_1 L_2} \tag{9}$$

**Table 2** Parameters of the WPT system.

| Parameters | $U_s$ (V) | $\omega$ (kHz) | $R_L$ (Ω) | $R_1$ (Ω) | $R_2$ (Ω) |
|---|---|---|---|---|---|
| Value | 85.0 | 85.5 | 25.0 | 1 | 1 |

## 3.2 Modeling of coils and pavement

To obtain the self-inductance and mutual inductance values and coupling coefficients of the coupling coils under different pavement layouts, the finite element models of the primary and secondary coils and pavement were established in Ansys Maxwell software. The coil model employed parameters from a previous study (Li et al., 2022). The primary coil featured a circular design with an inner diameter of 100 mm and an outer diameter of 250 mm. It was constructed from Litz wire, comprising 200 strands with a diameter of 2 mm each. This coil, incorporating 30 turns across two layers, was enhanced with 18 ferrite rods, each 10 mm wide and 3 mm thick, positioned behind it to augment the coupling effect. The secondary coil mirrored the primary in structure. The finite element modeling yielded a self-inductance value for the primary coil of 279.06 μH, equating to 112.0% of its physical counterpart's measured value. Similarly, the secondary coil's self-inductance from simulation was 279.09 μH, equating to 111.2% of the physical measurement. The incomplete connection of ferrite rods at the coil's corners led to magnetic leakage and a reduced self-inductance. The deviation between the results of the finite element model and measured values was acceptable, indicating that the models of coils were effective. When modeling the pavement, a rectangular structure with dimensions twice the outer diameter of the coil was used to fully encompass the magnetic field between the primary and secondary coils, with a thickness equal to half the distance between the coils. During the material attribution phase, there were two categories of materials: conventional pavement material and SMC material, both assumed to be homogeneous. These two materials were used in different zones of the pavement, as specified in the various layout configurations. Please refer to Section 3.3 for more details, and the simulation model of the coil and pavement under one of the layouts is shown in Fig. 2 (A) and (B). The relative permeability of SMC material was obtained by VSM testing. ‘AC-13’ was chosen as the conventional pavement material, which had a relative permeability of 1.049 (Li et al., 2022).

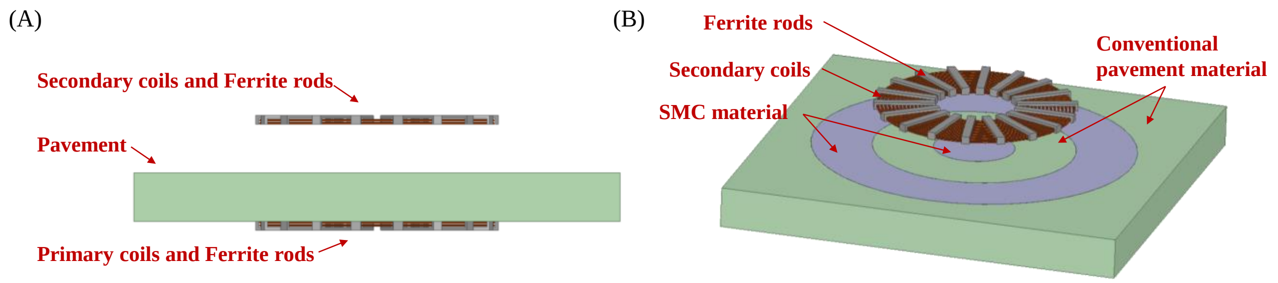


**Fig. 2.** The model of coils and pavement, including (A) the Front view of the finite element model, (B) the Three-dimensional view of the finite element model under one of the layouts.

### 3.3 Design principle of magnetized pavement

The essence of coupling of the primary and secondary coils is that the primary coil generates time-varying flux, which passes through the secondary coil. The magnetic flux shape diagram of the planar coil is shown in Fig. 3. Using SMC materials in locations traversed by the flux path can enhance the permeability of the pavement, although the exact of the flux path was unknown. Based on the inner and outer diameter of the coil and the extent of the magnetic field in the surrounding air medium, the pavement was segmented into seven regions, illustrated in Fig. 4. The first region, region1, corresponds to the hollow core region of the primary coil, making it circular with a radius equal to the primary coil's inner diameter. Regions 2 - 4 correspond to the wired region of the primary coil. Due to the uncertainty regarding the radiation range of the magnetic flux passing through the center of the primary coil, the wired region of the primary coil is evenly divided into three annular sections, denoted as regions 2, 3, and 4. This facilitates determining the magnetic flux range and the optimal structure of the magnetized pavement by varying the types of materials laid in each region. In order to explore the layout of the magnetized pavement outside the primary coil, the area extending beyond the primary coil to where the magnetic flux density attenuates to 0.0001T is divided into two sections, namely regions 5 and 6. Therefore, regions 5 and 6 are also annular. The area beyond region 6 is all marked as region 7. Table 3 shows the inner and outer radius of each region. The designation "$R_{in}$", "$R_{out}$" and "MF" represented the inner radius of the coil, the outer radius of the coil, and the region where the magnetic flux density outside the coil exceeded 0.0001 T, respectively. In each region, either conventional pavement material or SMC material was utilized, resulting in a total of nine different pavement layouts, as shown in Fig. 5.

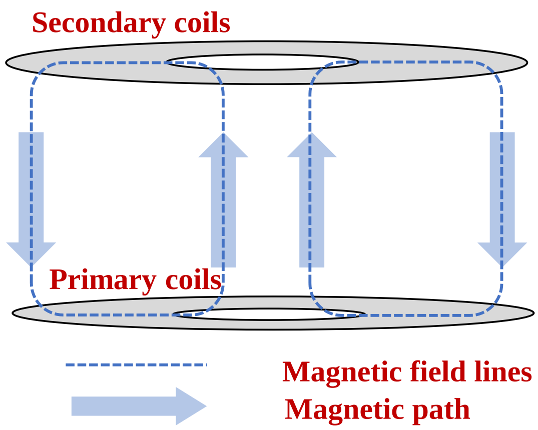


**Fig. 3.** Schematic diagram of the shape of the magnetic flux between primary and secondary coils.

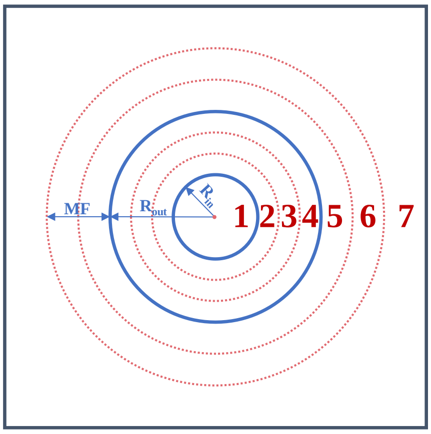


**Fig. 4.** The regional division of wireless charging pavement.

**Table 3** Dimensions of each region of the wireless charging pavement.

| Region | 1 | 2 | 3 | 4 | 5 | 6 | 7 |
|---|---|---|---|---|---|---|---|
| Inner radius | NA | $R_{in}$ | $(R_{out}+2*R_{in})/3$ | $(2*R_{out} + R_{in})/3$ | $R_{out}$ | $R_{out}$ + MF/2 | $R_{out}$ + MF |
| Outer radius | $R_{in}$ | $(R_{out} + 2*R_{in})/3$ | $(2*R_{out} + R_{in})/3$ | $R_{out}$ | $R_{out}$ + MF/2 | $R_{out}$ + MF | Boundary of the pavement |

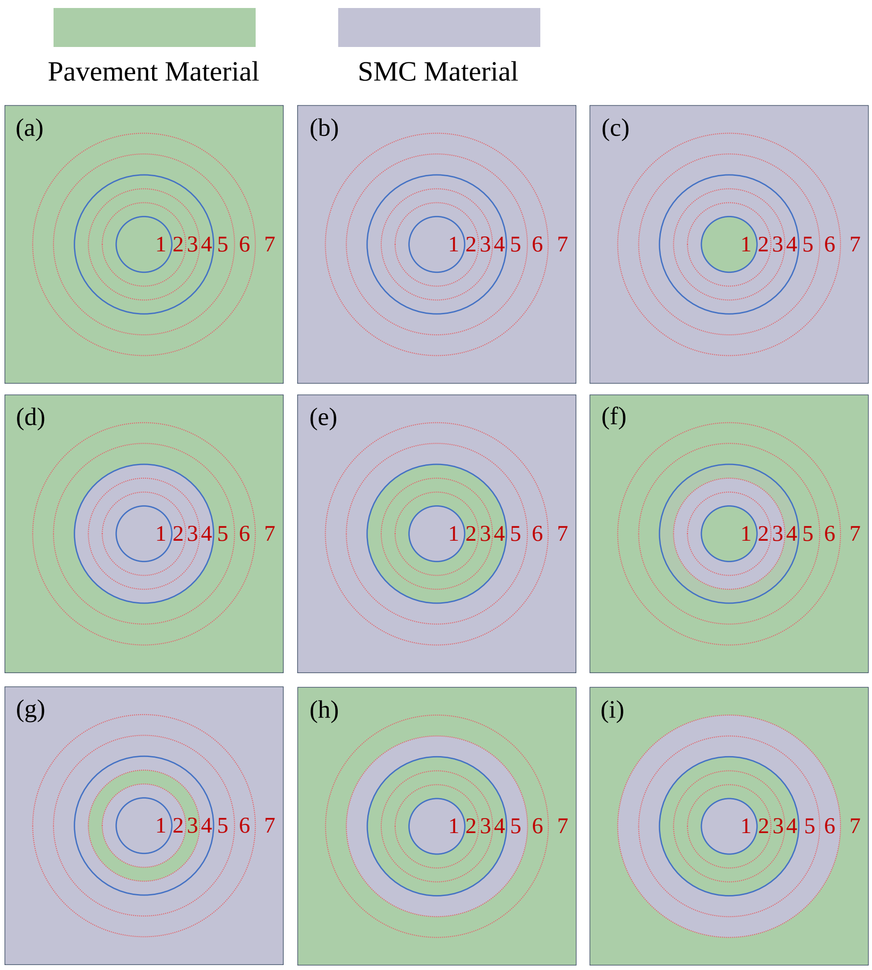


**Fig. 5.** Nine layout configurations of magnetized pavement including conventional pavement material and SMC material.

## 4 Results and discussions

### 4.1 Characteristics of raw materials

Table 4 presents the chemical composition of the three raw materials, and it can be seen that the most abundant element in the cement was Ca, in addition to Si, Al, Mn, and Fe. In Mn-Zn and Ni-Zn ferrite powders, Fe was the predominant element, comprising 73.747% and 70.981% of the oxide mass, respectively. Mn and Zn were the second and third most abundant elements in Mn-Zn ferrite powder, constituting 20.673% and 4.890% by mass of their oxides. Ni-Zn ferrite powder contained approximately 9% each of magnesium and zinc oxides, along with a small amount of Mn. The median particle sizes of cement, Mn-Zn, and Ni-Zn ferrite powders were 14.07 μm, 140.76 μm, and 3.75 μm, respectively, as illustrated in Fig. 6. The particle size of Ni-Zn ferrite was the smallest, predominantly falling within the range of 1-10 μm. Cement particles were primarily concentrated between 10-30 μm, while Mn-Zn ferrite exhibited the largest particle size, concentrated mainly between 100-200 μm. The difference in particle size distribution between Mn-Zn ferrite and Ni-Zn ferrite can also be seen in Fig. 7, where there are more small-sized particles in Ni-Zn ferrite. In terms of surface morphology, the shapes of Mn-Zn ferrite powder and Ni-Zn ferrite powder were similar, and both showed a spinel structure. Besides, VSM test results showed that the relative permeability of Mn-Zn ferrite was 31.104, and that of Ni-Zn ferrite was 41.185.

**Table 4** The chemical compositions of the raw materials (wt.%).

| Oxide contents | $Fe_2O_3$ | MnO | ZnO | $SiO_2$ | CaO | MgO | $Al_2O_3$ | NiO | CuO | $Co_3O_4$ | Remaining |
|---|---|---|---|---|---|---|---|---|---|---|---|
| Cement | 3.284 | 0.077 | 0.018 | 26.352 | 47.062 | 5.309 | 12.871 | 0 | 0 | 0 | 5.027 |
| Mn-Zn | 73.747 | 20.673 | 4.890 | 0.191 | 0.081 | 0.071 | 0.087 | 0 | 0 | 0.149 | 0.111 |
| Ni-Zn | 70.981 | 4.759 | 9.695 | 0.753 | 0.431 | 9.910 | 0.445 | 0.390 | 1.818 | 0.121 | 0.697 |

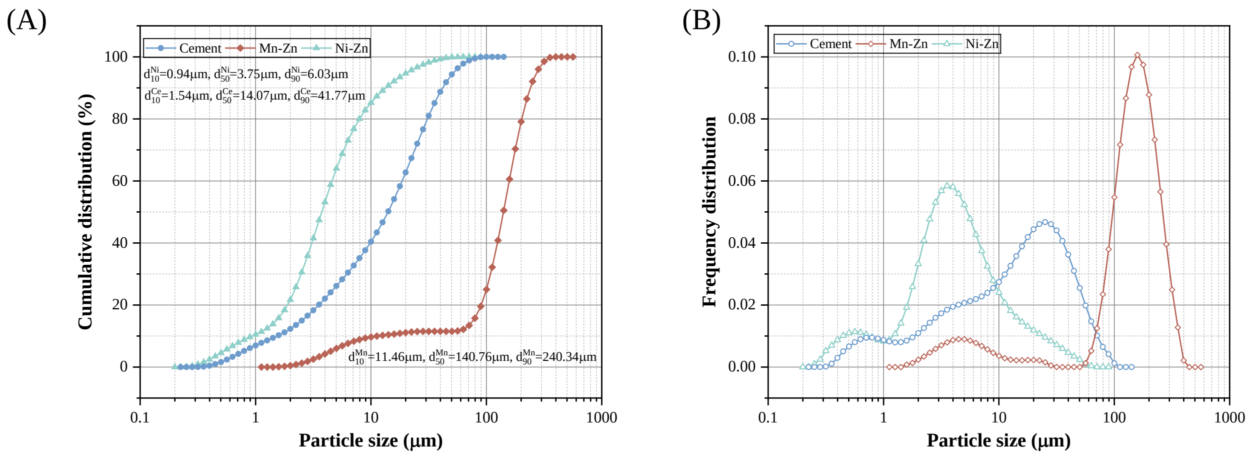


**Fig. 6.** Particle size distribution of cement, Mn-Zn, and Ni-Zn ferrite powders, including (A) Cumulative distribution curves, (B) Frequency distribution curves.

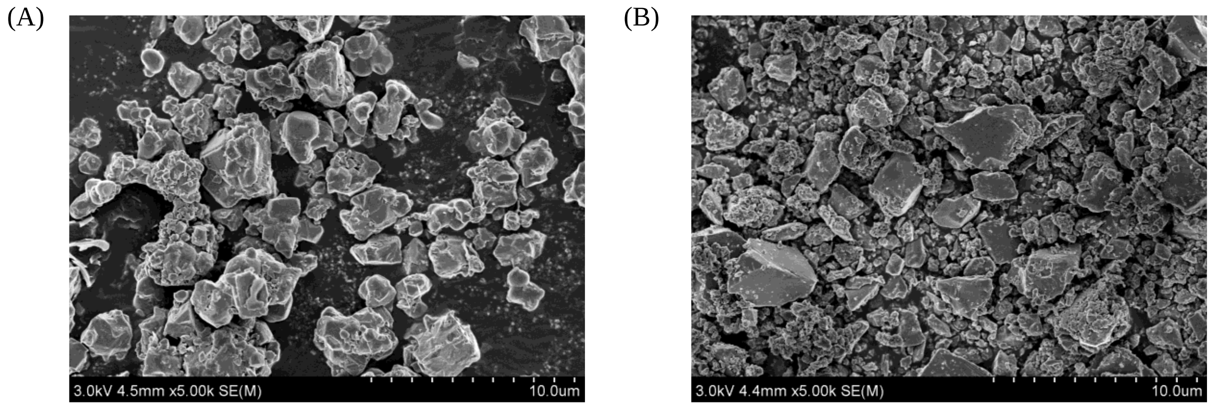


**Fig. 7.** Microstructural image of ferrite powders, including (A) Mn-Zn ferrite powders, (B) Ni-Zn ferrite powders.

### 4.2 Magnetic properties of SMC material

Fig. 8 presents the magnetic properties of SMC material species with varying water-solid ratios. It can be seen that the hysteresis loops exhibited a distinct S-shape and small coercivities, indicating significant soft magnetic behavior in the tested specimens (Schubert et al., 2019). The maximum magnetic susceptibility is the maximum slope of the hysteresis loop, which is dimensionless. The maximum relative permeability of the sample can be calculated, considering that it relates to the maximum magnetic susceptibility by adding 1. The relative permeability of specimens is shown in Fig. 9. When comparing SMC materials with the same ferrite content, those prepared with Ni-Zn ferrite powder demonstrated higher relative permeability compared to those prepared with Mn-Zn ferrite powder. This was due to the fact that the magnetic field inside the SMC was predominantly transmitted through magnetic powders, and as the VSM test results showed, Ni-Zn ferrite possessed inherently superior permeability properties.

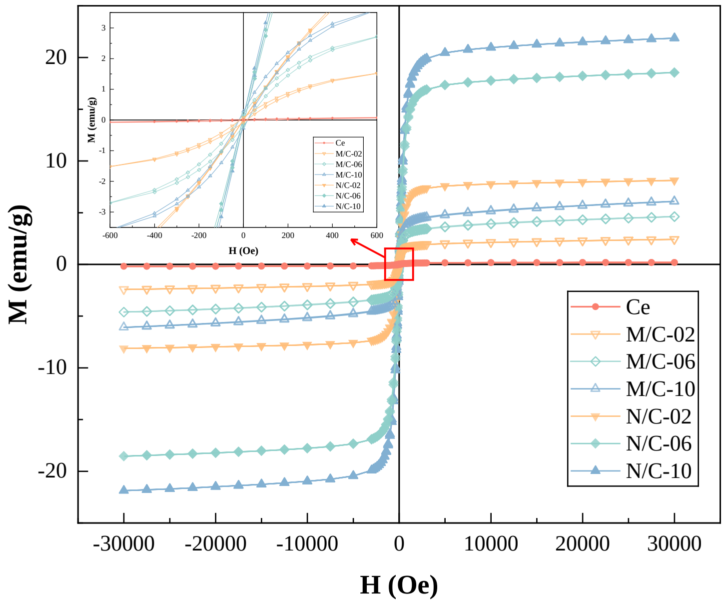


**Fig. 8.** Hysteresis loops of SMC materials.

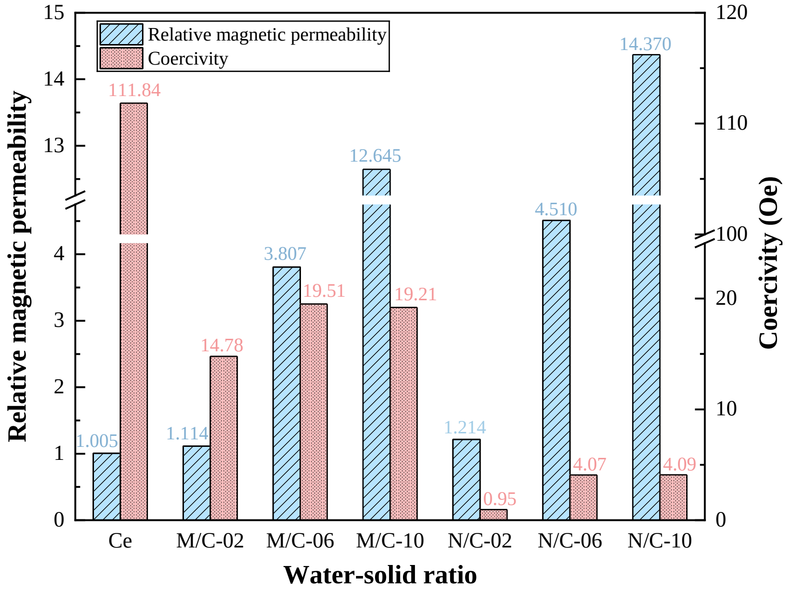


**Fig. 9.** Relative magnetic permeability and Coercivity of SMC materials.

The schematic diagram of the internal structure of the SMC material was shown in Fig. 10(A). The SMC material consisted of cement paste and ferrite powders. Ferrite powder is a type of ferrimagnetic material, consisting of electrons moving circularly around nuclei, thus forming ampere molecular currents (Arrigo et al., 2022; Sadhukhan and Deb, 2021). These ampere molecular currents give rise to electron orbital magnetic moments, denoted as $\overrightarrow{\mu_l}$. In addition to the orbital motion, electrons also possess spin, resulting in electron spin magnetic moments, represented by $\overrightarrow{\mu_s}$. The magnitudes of the total orbital magnetic moment $\overrightarrow{\mu_L}$ and the total spin magnetic moment $\overrightarrow{\mu_S}$ of the electrons are described by Eqs. (10)-(11). The vector sum of $\overrightarrow{\mu_L}$ and $\overrightarrow{\mu_S}$ forms electron magnetic moments $\overrightarrow{\mu_M}$, the source of material magnetism, as shown in Eq. (12) and Fig. 10(B). Compared to Mn-Zn ferrite, Ni-Zn ferrite contained more Ni, Zn, and Cu, which have larger electron magnetic moments. As a result, SMC material prepared with Ni-Zn ferrite exhibited greater magnetization intensity, as indicated in Eq. (13).

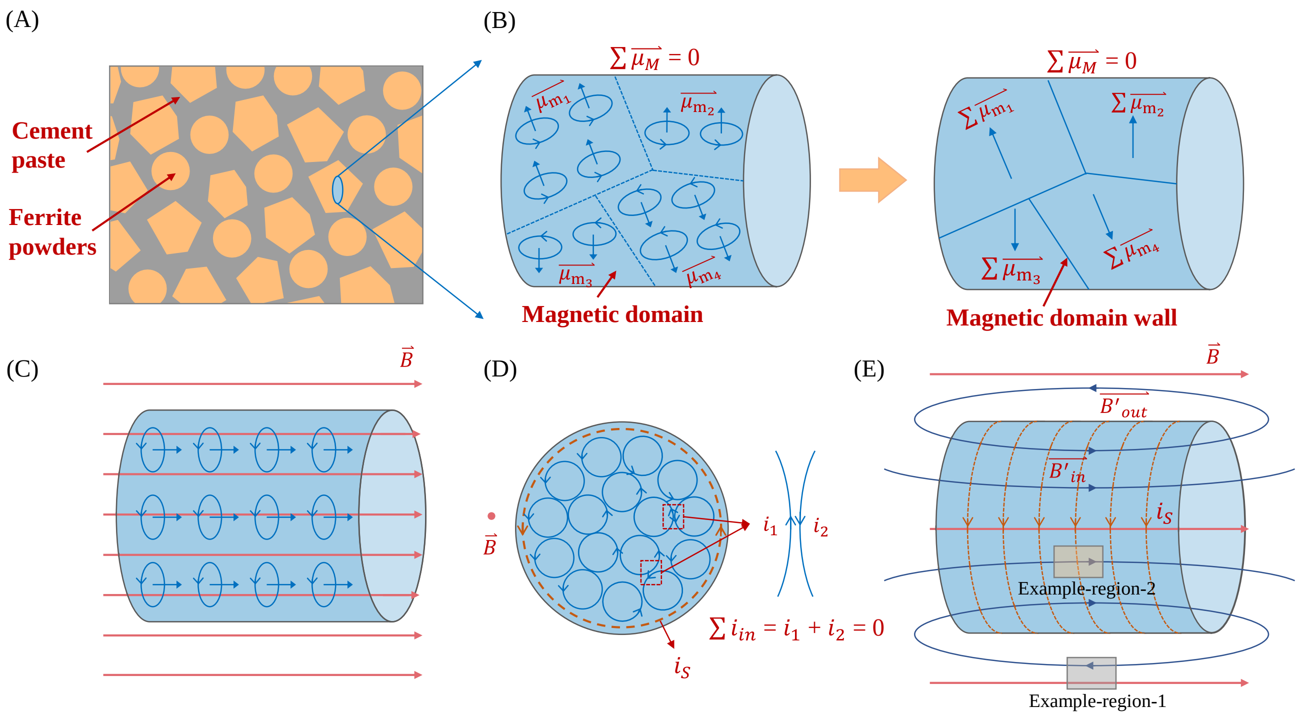


**Fig. 10.** Illustration of the magnetization behavior of the SMC material, including (A) Structural diagram of SMC material, (B) Internal domain distribution of ferrite powder without external magnetic field, (C) Magnetic moment of electrons in ferrite powder aligned along external magnetic field under external magnetic field, (D) Annular magnetizing current formed by ampere-molecular current on the surface of ferrite powder, (E) The induced magnetic field strengthens and weakens the external magnetic field inside and outside the ferrite powder particles.

$$\mu_L = \sqrt{L(L+1)}\mu_B \tag{10}$$

$$\mu_S = -\gamma_s \sqrt{S(S+1)\frac{h}{2\pi}} \tag{11}$$

$$\mu_M = g_J\sqrt{J(J+1)}\mu_B \tag{12}$$

$$M = \frac{\sum \mu_M}{\Delta V} \tag{13}$$

Where: $L$ is the total orbital angular momentum quantum number; $\mu_B$ is the Bohr magneton, with a magnitude of 9.2730e-24 A·m²; $\gamma_s$ is the gyromagnetic ratio of the electron spin; $S$ is the total spin quantum number; $h$ is the Planck constant; $g_J = 1 + \frac{J(J+1)+S(S+1)-L(L+1)}{2J(J+1)}$ is referred to as the Lande g-factor; $J$ represents the total angular momentum quantum number of an atom; $M$ is magnetization intensity; $\Delta V$ is the volume element.

Besides, during the spontaneous magnetization process, magnetic moments align within small regions, creating distinct magnetization regions known as magnetic domains, as depicted in Fig. 10(B). The boundaries between these domains are called domain walls. When an external magnetic field is applied, the magnetic moments align with the field direction, causing the domain walls to shift and eventually dissipate, as shown in Fig. 10(C). Therefore, in the process of enhancing the external magnetic field of paramagnetic materials, the domain wall energy needs to be overcome first. Due to its smaller particle size, Ni-Zn ferrite powder restricted the formation of magnetic domains, resulting in fewer domains. As a result, it required less energy to overcome domain walls, leading to higher permeability, consistent with the VSM test results.

For both kinds of ferrite powder, the relative permeability of SMC material gradually increased with the increase of ferrite powder content. The reason was that within the same volume, an increase in the proportion of the magnetic phase and a decrease in the proportion of the non-magnetic phase, as shown in Fig. 11, led to a reduction in the overall magnetic resistance of the magnetic flux path (Ma et al., 2023). Additionally, the synergistic enhancement of magnetic moments among magnetic particles contributed to the increased permeability of the composite material. As described above, after applying a magnetic field $\vec{B}$, the magnetic moments inside the SMC material aligned in the direction of the external magnetic field, as shown in Fig. 10(C). The adjacent ampere-molecular currents inside the cross-section canceled each other, and only those on the cross-section surface did not cancel, thus forming a ring magnetizing current on the surface, as shown in Fig. 10(D). Due to the existence of a ring-magnetizing current, an additional magnetic field $\overrightarrow{B'}$ was generated, with the same direction as $\vec{B}$ inside the magnetic powder, labeled as $\overrightarrow{B'_{in}}$, and in the opposite direction of $\vec{B}$ outside the magnetic powder, labeled as $\overrightarrow{B'_{out}}$, as shown in Fig. 10(E). The synergistic enhancement of magnetic moments among magnetic particles can be proved by comparing the sum of magnetic fluxes in Example-region-1 and Example-region-2 at low and high content. At lower content of ferrite powder, Example-region-1 consisted primarily of non-magnetic material. The magnetic field in this region, $\overrightarrow{B_{L-1}}$, was the sum of $\vec{B}$ and $\overrightarrow{B'_{out}}$, as shown in Eq (14). The magnetic field in Example-region-2, $\overrightarrow{B_{L-2}}$, was the sum of $\vec{B}$ and $\overrightarrow{B'_{in}}$. The sum of the magnetic flux of the two regions is shown in Eq (16). As the powder content increased, the reduced spacing between ferrite particles led to the distribution of magnetic particles within Example-region-1. In this case, the total magnetic field, labeled as $\overrightarrow{B_{H-1}}$ is comprised of $\vec{B}$, $\overrightarrow{B''_{in}}$, and $\overrightarrow{B'_{out}}$. The magnetic field in Example-region-2, $\overrightarrow{B_{H-2}}$, increased the $\overrightarrow{B''_{out}}$ generated by new magnetic particles on the basis of the previous.

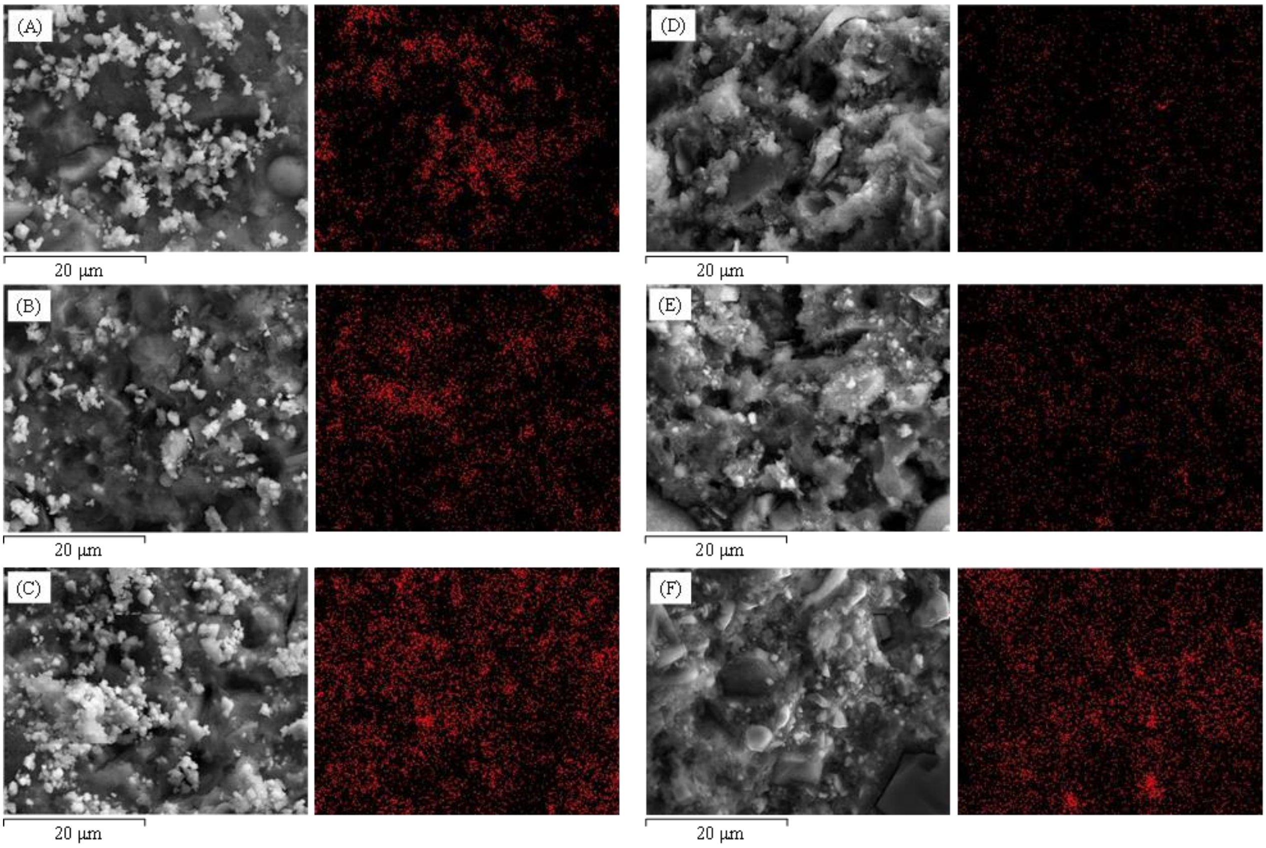


**Fig. 11.** Distribution of Mn element represented by red color in SMC materials tested by EDS, including (A) M/C-02, (B) M/C-06, (C) M/C-10, (D) N/C-02, (E) N/C-06, (F) N/C-10.

$$\overrightarrow{B_{L-1}} = \vec{B} + \overrightarrow{B'_{out}} \quad (14)$$

$$\overrightarrow{B_{L-2}} = \vec{B} + \overrightarrow{B'_{in}} \quad (15)$$

$$\Phi_L = \iint_{S_1} \overrightarrow{B_{L-1}} \cdot ds_1 + \iint_{S_2} \overrightarrow{B_{L-2}} \cdot ds_2 \quad (16)$$

$$\overrightarrow{B_{H-1}} = \vec{B} + \overrightarrow{B''_{in}} + \overrightarrow{B'_{out}} \quad (17)$$

$$\overrightarrow{B_{H-2}} = \vec{B} + \overrightarrow{B'_{in}} + \overrightarrow{B''_{out}} \quad (18)$$

$$\Phi_H = \iint_{S_1} \overrightarrow{B_{H-1}} \cdot ds_1 + \iint_{S_2} \overrightarrow{B_{H-2}} \cdot ds_2 \quad (19)$$

It was assumed that, for a given applied magnetic field, the additional magnetic fields generated by different particles of the same substance would be identical. Thus, $\overrightarrow{B''_{in}}$ was equal to $\overrightarrow{B'_{in}}$, and $\overrightarrow{B''_{out}}$ was equal to $\overrightarrow{B'_{out}}$. The difference between the two magnetic fluxes was calculated as:

$$\Delta\Phi = \Phi_H - \Phi_L = \iint_{S_1} \overrightarrow{B'_{in}} \cdot ds_1 - \iint_{S_2} \overrightarrow{B'_{out}} \cdot ds_2 \quad (20)$$

$\overrightarrow{B'_{out}}$ dispersed and gradually attenuated while propagating outside the magnetic particles, remaining consistently smaller than $\overrightarrow{B'_{in}}$. Additionally, the non-magnetic phase had a larger integral area when the ratio of ferrite powder to cement was less than 1. This discrepancy led to a greater magnitude of magnetic flux $\Phi_H$

than $\Phi_L$, indicating an enhanced synergistic effect among the magnetic particles as the content of magnetic particles increased.

Regarding the coercivity shown in Fig. 9, the cement paste exhibited the highest coercivity, measuring 111.84 Oe. This high value suggested that the cement paste did not possess soft magnetic characteristics. For SMC materials, those prepared with Ni-Zn ferrite powder exhibited lower coercivity compared to those using Mn-Zn ferrite. Eq (21) (Varga et al., 2006) derives the relationship between coercivity and magnetic domain wall energy, explaining the observed results by Ni-Zn ferrites' smaller domain wall energy and particle size. When the content of ferrite powder increased, the coercivity of the SMC materials gradually increased and reached a stable level. This was attributed to the increased number of magnetic particles and magnetic domain walls (Gao et al., 2023). Additionally, as the ferrite powder content increased, the pinning effect of the non-magnetic phase on the coercivity weakened (Ji et al., 2022; Zhou et al., 2020).

$$H_{eff} = \frac{\gamma}{J_s d}(1 + \frac{9}{8} N \alpha D S_V) \tag{21}$$

Where: $H_{eff}$ is the coercivity; $\gamma$ is the magnetic domain wall energy; $J_S$ is the magnetic polarization strength; $d$ is the magnetic domain wall width; $N$ is the demagnetization factor; $\alpha$ is the parameter related to the domain shape; $D$ is the magnetic particle diameter; $S_V$ is the magnetic domain wall area per unit volume.

Meanwhile, Fig. 12 presents that the saturation magnetization strength of SMC material in descending order: N/C-10＞N/C-06＞N/C-02＞M/C-10＞M/C-06＞M/C-02＞Ce. The type of material was identified as the primary influencing factor, with the content of ferrite powder being the secondary factor. This can be attributed to the strong magnetic moments present in the Ni-Zn ferrite powder. When the applied magnetic field is strong enough, the magnetic moments within the specimens fully align with the direction of the external magnetic field, leading to the saturation of magnetization strength.

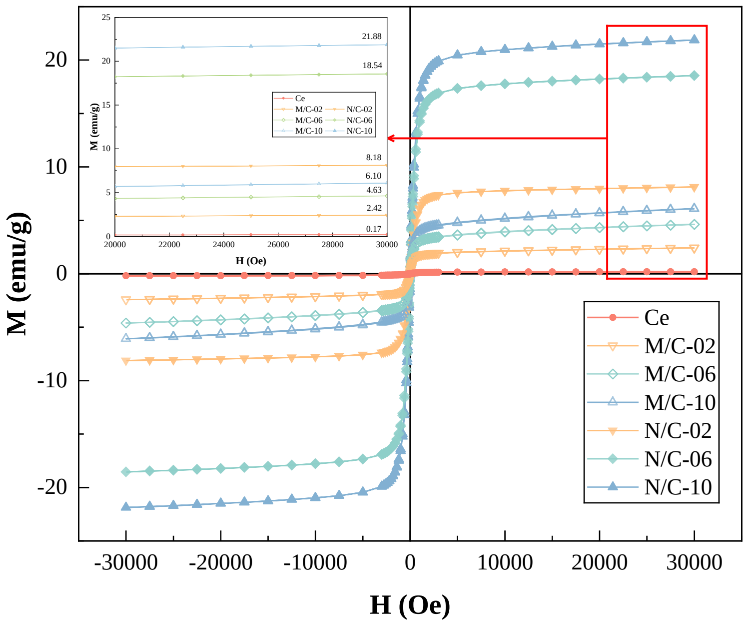


**Fig. 12.** Saturation magnetization strength of SMC materials.

### 4.3 Mechanical properties of SMC material

As can be seen from Fig. 13, incorporating magnetic materials into cement reduces both the flexural and compressive strengths of SMC materials. The SMC material prepared with both types of ferrite powders exhibited a pattern where strength decreased more rapidly with an increase of ferrite content. Among all SMC materials, the highest compressive and flexural strengths were observed when the Mn-Zn ferrite powder to cement ratio was 0.2, with flexural strength at 4.0 MPa and compressive strength at 36 MPa, marking decreases of 0.5 MPa and 11.8 MPa, respectively, compared to pure cement specimens. Materials with Mn-Zn ferrite powder to cement ratios of 0.6 and Ni-Zn ferrite powder to cement ratios of 0.2 showed nearly identical flexural strengths of 3.8 MPa and 3.7 MPa, respectively, closely following M/C-06. However, M/C-06's compressive strength decreased more significantly, to 22.3 MPa, compared to 31.8 MPa for N/C-02. As the ferrite content increased, M/C-10 maintained a certain level of strength, with a flexural strength of 2.5 MPa and a compressive strength of 8.6 MPa. Yet, as the Ni-Zn ferrite powder to cement ratio reached 0.6, the strength of the SMC rapidly declined to almost negligible.

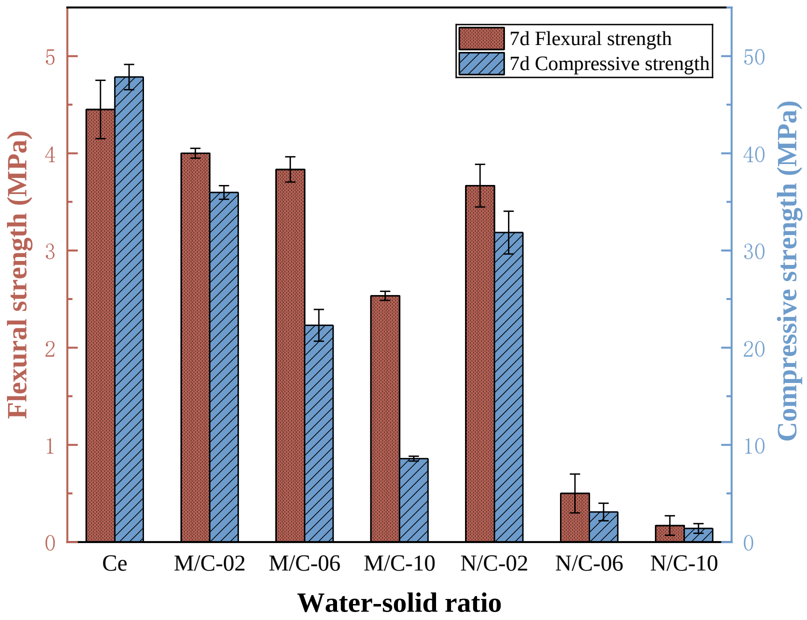


**Fig. 13.** Mechanical properties of SMC materials.

For the inorganic cementitious materials containing fine aggregates, the strength evolution mechanism is mainly related to the internal chemical reaction process and the interfacial connection between fine aggregates and the inorganic cementitious material matrix. It can be seen from Fig. 14(A) that an obvious calcium silicate hydrate (C-S-H) gel structure was formed in the cement paste. Fig. 14(B)-(G) showed that there was no apparent interfacial connection between the ferrite powder particles and the cement's hydration product; instead, the ferrite powder particles adhered to the surface of the C-S-H gel. Therefore, the strength of the SMC material mainly depended on the hydration products of cement. In the microstructures of M/C-02, M/C-06, and N/C-02 featured a more distinct needle-like C-S-H gel structure, while in the microstructures of M/C-10, N/C-06, and N/C-10, the C-S-H gel structure was significantly reduced. This change resulted from the increased ferrite powder content, which reduced the cement content, leading to a decrease in the production of the C-S-H gel structure and consequently affecting the strength of SMC materials. Additionally, SMC prepared with Mn-Zn ferrite generally exhibited higher strength than those prepared using Ni-Zn ferrite powder. This difference is attributed to the smaller particle size of Ni-Zn ferrite powder compared to Mn-Zn ferrite powder, resulting in a stronger encapsulation effect on the C-S-H gel and consequently reducing the strength of the SMC material.

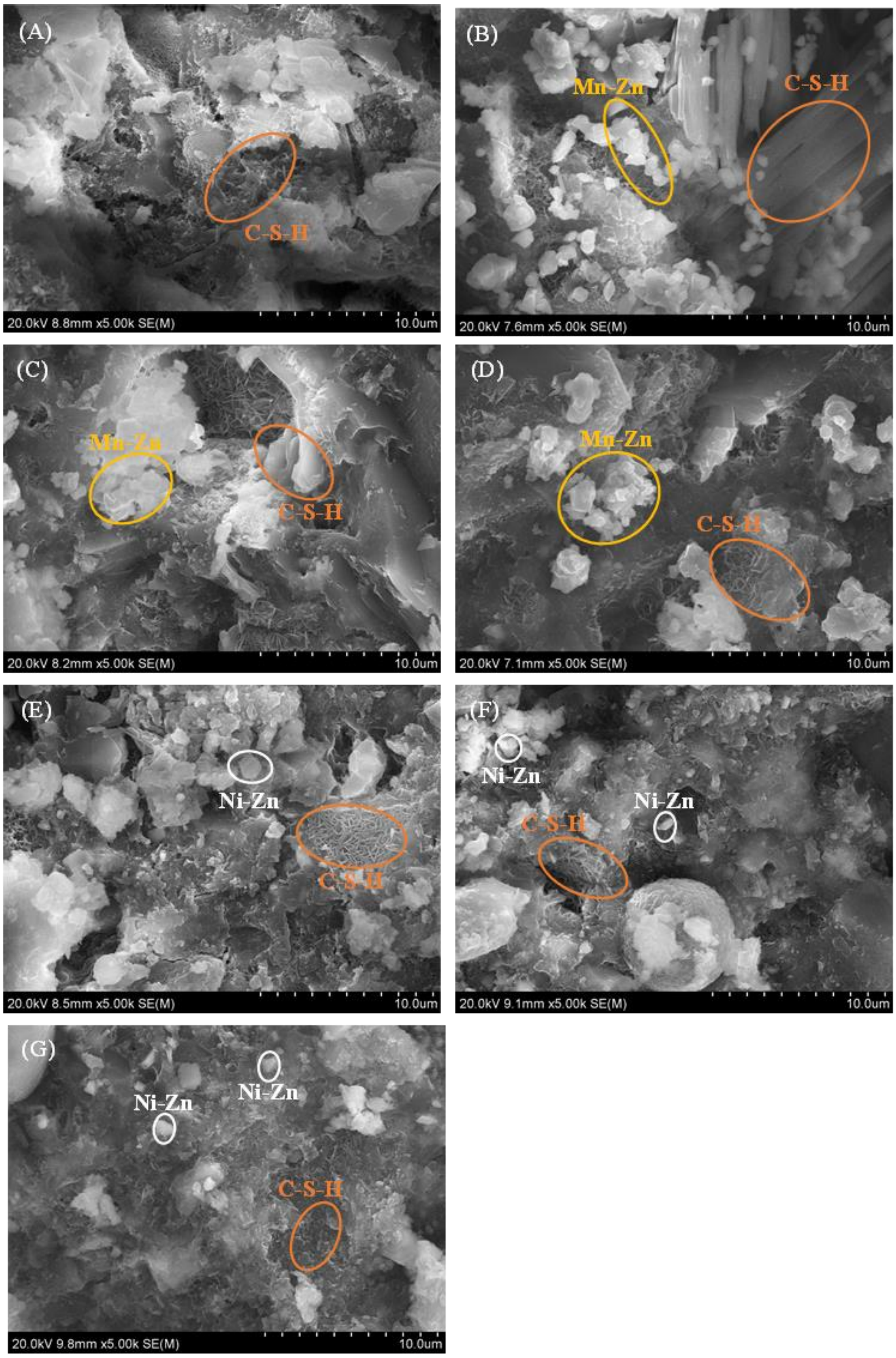


**Fig. 14.** Microstructure of SMC materials, including (A) Ce, (B) M/C-02, (C) M/C-06, (D) M/C-10, (E) N/C-02, (F) N/C-06, (G) N/C-10.

### 4.4 Influence of magnetized pavement on WPT system

#### 4.4.1 Setting of magnetized pavement

The performance of the coils under nine magnetized pavement layouts is shown in Fig. 15. When SMC materials were used in various areas of the pavement structure, the self-inductance of the primary coil and the secondary coil was enhanced to different degrees. The mutual inductance decreased under layouts (b) and (f), but increased under other layouts. The coupling coefficient between coils varied, showing both increases and decreases across different layouts.

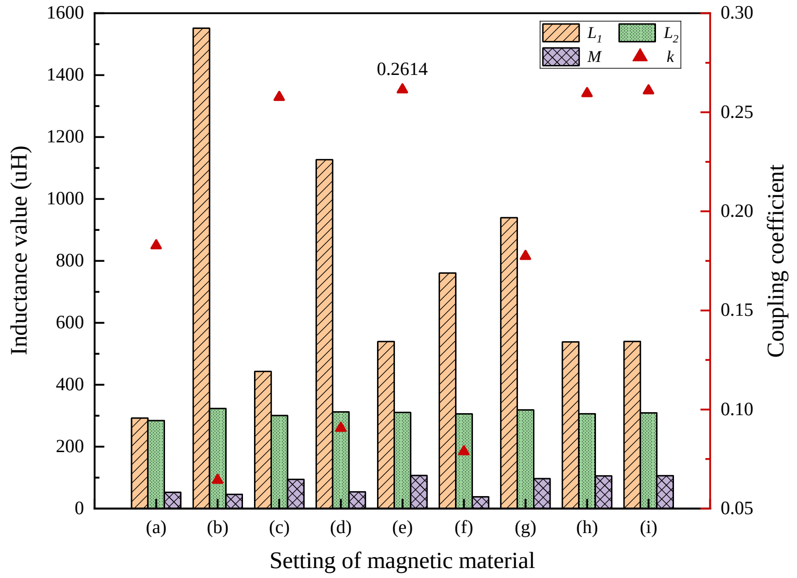


**Fig. 15.** Coil self-inductance, mutual inductance, and coupling coefficient of coils under different layouts.

By comparing the layouts (a) and (c), it is found that the coil coupling coefficient increased significantly when the magnetic materials were placed in the coil's empty core position, that is, in region-1. By comparing (b), (e) and (g), (c) and (d), (a) and (f), it can be found that the coil coupling coefficient decreased when the magnetic materials extended into the coil's wired area. The greater the area covered by the SMC materials, the more the coil coupling coefficient decreased. By comparing the layout (c), (h), (i), and (e), it can be observed that employing magnetic material outside the primary coil could enhance the degree of coil coupling. Notably, an increased surface area of the magnetic material led to a more conspicuous enhancement effect. This phenomenon implied the presence of a magnetic flux pathway both inside the empty core and outside the primary coil, where the introduced magnetic material facilitates magnetic conduction. By contrast, there was only a small amount of stray magnetic flux in the wired area, that is, in region-2-3-4. The magnetic materials placed in the wired area cause the magnetic inductive lines to disperse transversely, acting as a shield, as reflected in the cloud diagrams for layouts (b) and (d). Therefore, the layout of (e) was optimal among all the layouts, with the highest coupling coefficient between coils (0.2614). It can also be seen from the cloud diagram in Fig. 16 that under the layout of (e), an obvious magnetic flux path was formed at the empty core position of coils.

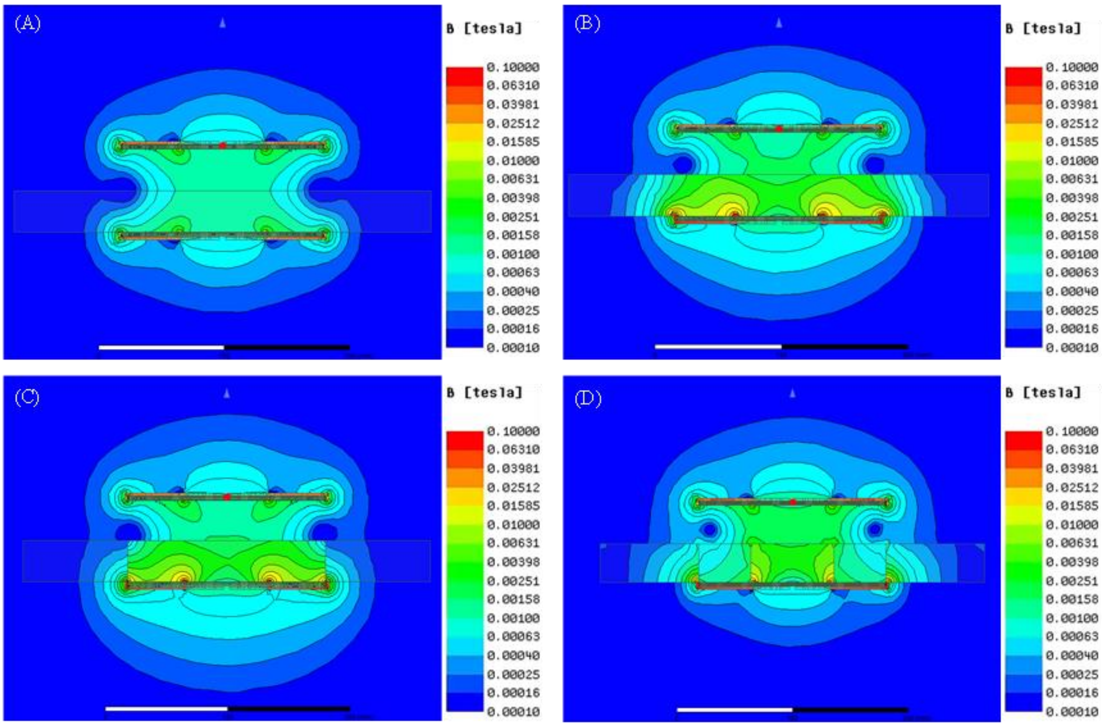


**Fig. 16.** Magnetic field cloud diagram between coils under different layouts, including (A) Layout of (a), (B) Layout of (b), (C) Layout of (d), (D) Layout of (e).

Fig. 17 shows the output power and transmission efficiency of the system under different layouts of SMC materials. Except for layouts (b) and (f), which completely covered the primary coil area, thereby shielding the magnetic field, all other magnetized pavement layouts demonstrated an improvement in system efficiency. This enhancement is advantageous in terms of reducing energy waste, promoting energy conservation, and mitigating carbon emissions. The highest efficiency, 95.40%, was achieved with the (e) or (i) layout, representing an efficiency improvement of 2.26% compared to using all pavement materials. The variation pattern of the output power relative to the layout of magnetic materials was exactly opposite to that of efficiency. As the transmission efficiency increased, the output power decreased, yet the absolute value of the energy loss experienced a reduction, which is beneficial for energy conservation. According to Eq. (8), the output power is directly proportional to the power supply voltage. By increasing the voltage of supply power, the output power of the system can be enhanced while keeping the transmission efficiency unchanged. Therefore, when selecting the layout of magnetized pavement, the focus should primarily be on the transmission efficiency of the system. It should be noted that (i) layout used less SMC material than (g) layout. Considering that SMC materials are costlier than standard pavement materials, layout (i) was recommended for its economic efficiency.

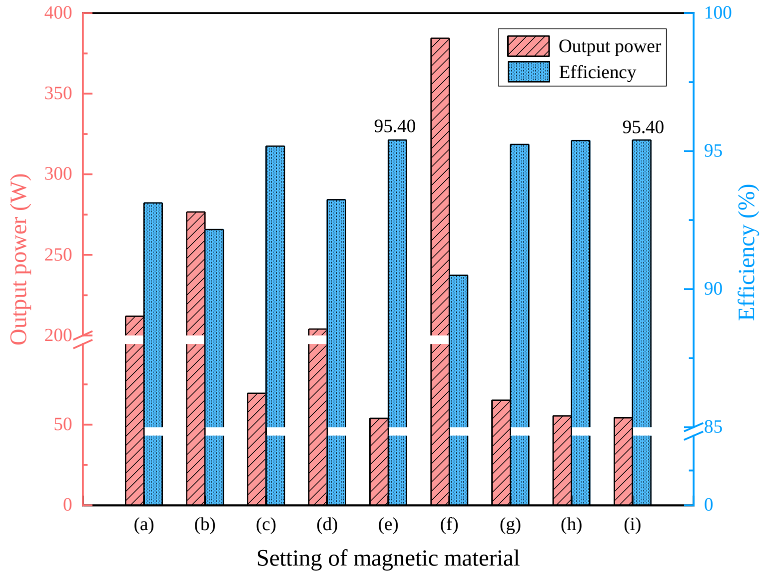


**Fig. 17.** Output power and transmission efficiency of WPT system under different layouts.

### 4.4.2 Types of SMC material

Under the layout of (i), the influence of the type of SMC material on the performance of the WPT system was explored. The results are shown in Table 5. Compared to cement paste, the use of SMC material significantly improved the self-inductance, mutual inductance, and coupling efficiency of coils, achieving maximum increases of 90%, 108.2%, and 44.8%, respectively. When the ferrite powder concentration in SMC material remained constant, SMC material prepared with Ni-Zn ferrite powder had a more significant effect on enhancing the self-inductance, mutual inductance, and coupling coefficient of the coils compared to those made with Mn-Zn ferrite powder. For instance, at a ferrite powder to cement mass ratio of 0.6, employing M/C-06 and N/C-06 type SMC material in magnetized pavement resulted in primary coil self-inductances of 401.50 μH and 421.01 μH, respectively, with coupling coefficients of 0.219 and 0.226. Moreover, as the ferrite powder content in SMC increased, there was a gradual enhancement in the coils' self-inductance, mutual inductance, and coupling coefficients. Specifically, the employment of N/C-10 material facilitated the highest mutual inductance and coupling coefficient, recorded at 109.81 μH and 0.265, respectively. Following this, when M/C-10 was used, the mutual inductance and coupling coefficient between coils were 106.54 μH and 0.261, respectively. The enhancement was positively correlated with the relative magnetic permeability of the material. Eqs. (22) and (23) represent the theoretical calculation for coil self-inductance and mutual inductance, where $N_L$ is the number of turns of coils, $r$ is the radius of coils, $a$ is the winding radius, $N_1$ and $r_1$ are the number of turns and radius of the primary coil, $N_2$, and $r_2$ are the number of turns and radius of the secondary coil, respectively. When the above parameters remain constant, self-inductance and mutual inductance depend on the relative permeability of the ambient medium around the coil ($\mu_r$), which explains the physical mechanism behind the varying enhancement effects of SMC material on the performance of coils.

**Table 5** The performance of the WPT system using different types of SMC material.

| Mixture | Ce | M/C-02 | M/C-06 | M/C-10 | N/C-02 | N/C-06 | N/C-10 |
|---|---|---|---|---|---|---|---|
| $L_1$ (μH) | 291.88 | 299.00 | 401.50 | 539.94 | 304.80 | 421.01 | 554.71 |
| $L_2$ (μH) | 286.51 | 288.17 | 297.87 | 308.83 | 289.1 | 300.16 | 309.78 |
| $M$ (μH) | 52.74 | 54.22 | 75.83 | 106.54 | 55.42 | 80.41 | 109.81 |
| $k$ | 0.183 | 0.185 | 0.219 | 0.261 | 0.187 | 0.226 | 0.265 |
| $P$ (W) | 211.12 | 200.46 | 105.53 | 54.27 | 192.31 | 94.15 | 51.13 |
| $\eta$ (%) | 93.14 | 93.29 | 94.67 | 95.40 | 93.41 | 94.83 | 95.44 |

$$L_{1/2} = \mu_r \mu_0 r {N_L}^2 \left( ln\left(\frac{8r}{a}\right) - 1.75 \right) \tag{22}$$

$$M = \frac{\pi}{2} \mu_r \mu_0 \frac{\sqrt{N_1 N_2 (r_1 r_2)^2}}{T^3} \tag{23}$$

Additionally, as the types of SMC material varied, the efficiency changed similarly to the mutual inductance, while the output power varied inversely. The variation was consistent with Eqs. (8) and (9). When N/C-10 was used, the WPT system achieved its highest efficiency of 95.44%, marking a 2.3% improvement over cement paste. The second and third highest transmission efficiencies were 95.40% and 94.67%, respectively, achieved when using M/C-10 and M/C-06. Considering the relatively low mechanical strength of specimen M/C-10 and N/C-10, it is recommended to employ M/C-06 SMC material for laying the magnetized pavement.

### 4.4.3 Verification by WPT system test platform

To verify the effect of magnetized pavement on enhancing the performance of WPT system, a physical experiment platform of WPT system was built to carry out the tests, as shown in Fig. 18. The test system adopted SS topology structure comprising a DC power supply, primary inverter, primary compensation capacitor, primary coil, secondary coil, secondary compensation capacitor, secondary rectifier, electronic load, and two oscilloscopes. Among them, the primary inverter utilized a full-bridge inverter circuit, while the secondary rectifier employed a full-bridge rectifier circuit. The structure of the primary and secondary coils mirrored that described in Section 3.2, with a transmission distance of 100 mm. The value of DC power supply, frequency and electric load were set according to those specified in Table 2, and the compensated capacitance value was determined using Eq. (5). Voltage and current in the primary and secondary circuit were measured using the oscilloscopes. The power and transmission efficiency of the WPT system were tested when the whole pavement material specimen and the magnetized pavement specimen were inserted to replace part of the air medium, and the energy loss was calculated. The whole pavement material specimen was made of AC-13 asphalt mixture, and the structure form was corresponding to the layout (a) in Fig. 5. Meanwhile, the magnetized pavement specimen was made of AC-13 asphalt mixture and M/C-06 SMC material, and the structure form was corresponding to the layout (i) in Fig. 5. Both types of specimens measured 500 mm in length and width, with a thickness of 50 mm. Detailed dimensions of the magnetized pavement specimen are illustrated in Fig. 18.

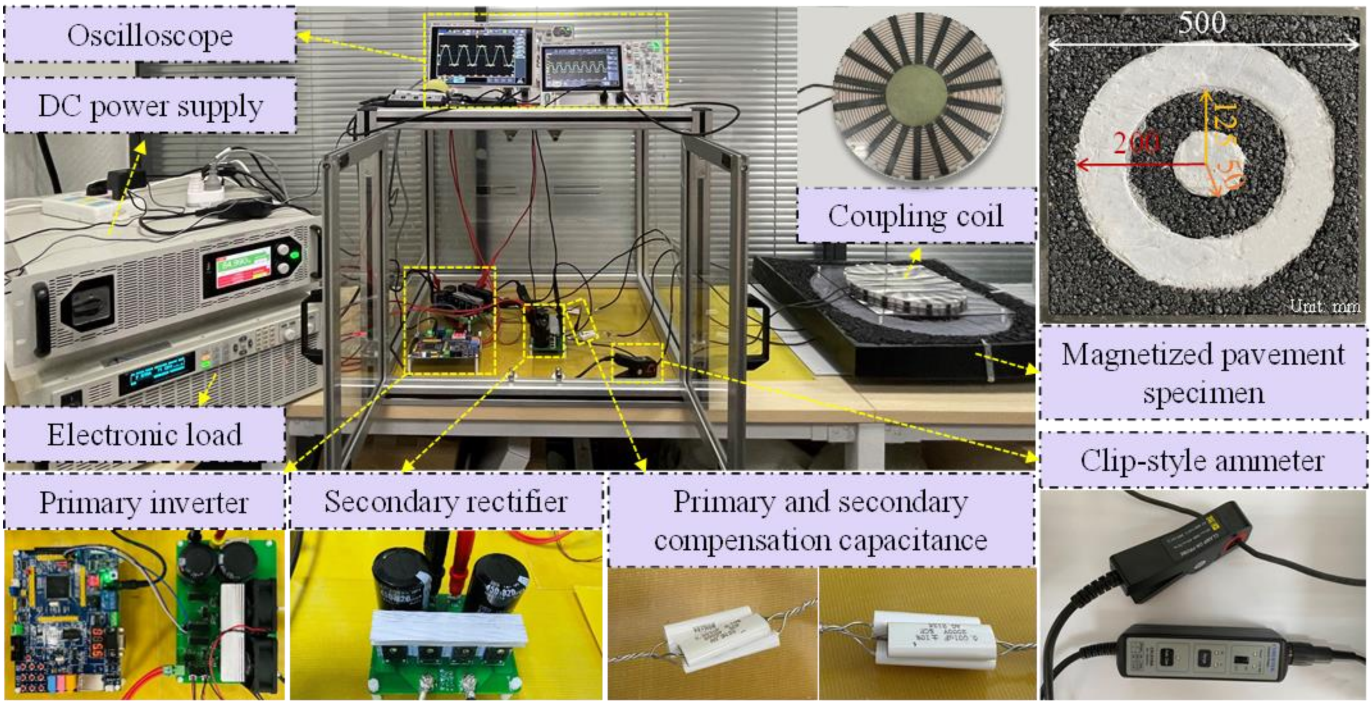


**Fig. 18.** WPT system test platform.

During testing, the primary and secondary circuits were initially adjusted to the resonant state, and judgment was made based on whether the waveform displayed on the oscilloscope resembles a square wave. Fig. 19 depicts the voltages and currents of the primary and secondary circuits of the WPT system with the whole pavement material specimen which also indicated their attainment of resonance. Fig. 20 depicts those of the WPT system with the magnetized pavement specimen.

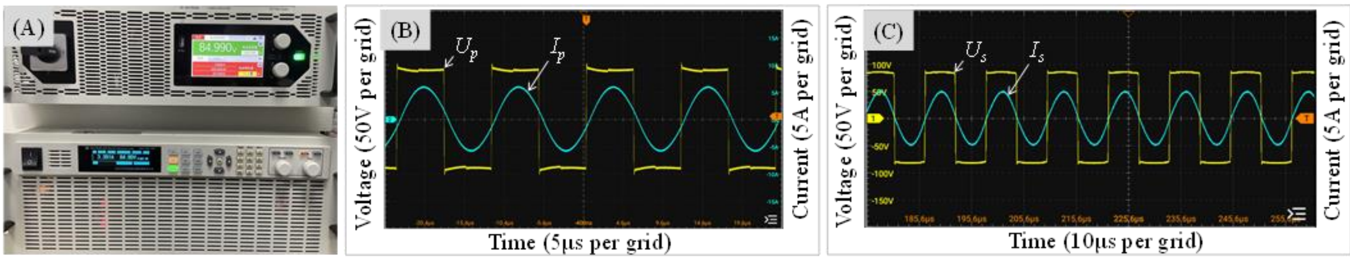


**Fig. 19.** The performance of WPT system with the whole pavement material specimen, including (A) Input and output voltages and currents, (B) Voltage and current waveforms of primary side circuit, (C) Voltage and current waveforms of secondary side circuits.

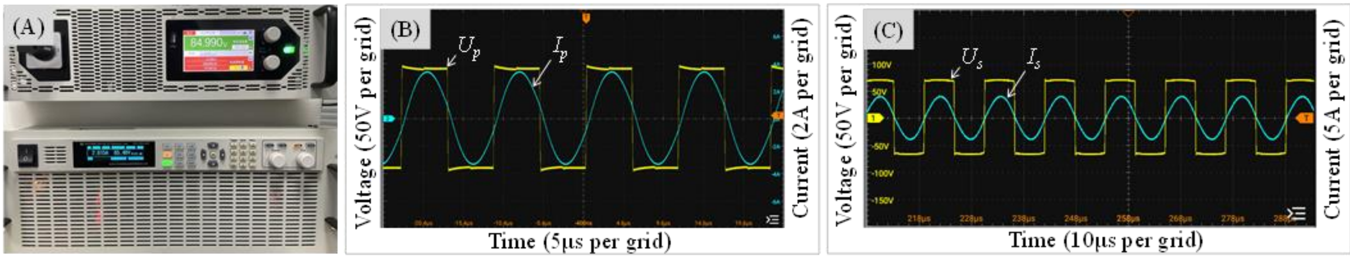


**Fig. 20.** The performance of WPT system with the magnetized pavement specimen, including (A) Input and output voltages and currents, (B) Voltage and current waveforms of primary side circuit, (C) Voltage and current waveforms of secondary side circuits.

With the whole pavement material specimen, the input power of the WPT system was 325.6 W, with an output power of 287.9 W, a transmission efficiency of 88.42%, resulting in an energy loss of 37.7 W. When utilizing magnetized pavement integrated with M/C-06 material in accordance with layout (i), the system exhibited an input power of 190.8 W and the output power of 171.3 W. The transmission efficiency was improved to 89.78%, which was 1.36% higher than that with pavement material, with an energy loss of 19.5 W. To equalize the output power between the two types of specimens, the system's power supply voltage should be raised when utilizing magnetized pavement. This adjustment did not affect the system's transmission efficiency, which remained at 89.78%, and led to an energy loss of 33.3 W, lower than with the whole pavement material. The test results confirmed that the incorporation of magnetized pavement was effective in improving the efficiency of WPT system and reducing energy loss, aligning with the simulation results. The discrepancies between the test results and the theoretical calculations were due to the omission of the primary inverter and secondary rectifier, as well as wire resistance, in the theoretical model.

## 5 Conclusions

In the field of electric vehicle charging, WPT technology will play a crucial role in the future. This study developed a novel magnetic material, SMC material, intended to replace the traditional pavement material. By designing SMC material layouts, conventional pavement can be transformed into a surface with magnetic field inducing function, referred to as wireless charging magnetized pavement. The innovative magnetized pavement can enhance the magnetic field transmission from the primary to the secondary coil, thus improving the transmission efficiency of the electric vehicle WPT system and reducing the loss of energy, so as to achieve the purpose of energy saving. With the maturation of magnetized pavement technology for wireless charging, it is expected that in the future, electric vehicles will be able to charge while on the move, promoting the widespread adoption of electric vehicles and contributing to carbon net zero. Moreover, it will foster the growth of intelligent transportation infrastructure, significantly contributing to the realization of sustainable transportation. The following conclusions were obtained:

1. The addition of cement as a matrix showed that both Ni-Zn and Mn-Zn ferrite powders increased the relative magnetic permeability of SMC materials proportionally with the ferrite powder content. The highest recorded relative permeability among the SMC materials was 14.370, when the ratio of Ni-Zn ferrite powder to cement powder was 1. The mixture with the highest ferrite powder content that maintains acceptable strength is the M/C-06.

2. Through the design of the SMC material layout, it was found that in magnetized pavement, the placement of the SMC material inside the core region and outside the coil area contributed to an improved coupling coefficient between the coils. Conversely, when the SMC material was placed within the wired region, the coupling degree between the coils was weakened. The layout (i) proposed in this paper is the recommended form for magnetized pavement.

3. The enhancement was positively correlated with the relative magnetic permeability of the SMC material. When using the N/C-10 material, the WPT system achieved the highest transmission efficiency. Given the balance between efficiency and mechanical properties, the M/C-06 SMC material is recommended for constructing magnetized pavement.

4. A WPT system test platform was established to verify the effect of magnetized pavement. Substituting the air medium with magnetized pavement made of M/C-06 resulted in a system transmission efficiency of 89.78%, surpassing the efficiency achieved when the whole pavement material was utilized by 1.36%. This finding underscores the energy-saving advantages of employing magnetized pavement in WPT technology.

Although integrating SMC material into magnetized pavement can improve the transmission efficiency of WPT systems for electric vehicles and conserve energy, this paper still has limitations. Embedding an SMC material layer into the pavement structure may compromise mechanical integrity. Future studies should focus on enhancing the deformation compatibility between SMC material and pavement material. This objective can be realized by designing the structural form of the connecting area to mitigate point load effects and by incorporating viscoelastic materials to buffer the interface between the two materials.

## CRediT author statement

**Yanjie Li**: Methodology, Data curation, Writing- Original draft preparation. **Feng Li:** Conceptualization, Supervision, Project administration, Funding acquisition. **Siqi Zhou**: Visualization, Writing - Original Draft, Writing - Review & Editing. **Xiaolei Ma**: Writing- Reviewing and Editing, Supervision. **Yue Hou:** Writing- Reviewing and Editing

## Declaration of Competing Interest

The authors declare that they have no known competing financial interests or personal relationships that could have appeared to influence the work reported in this paper.

## Acknowledgment

This work was supported by National Natural Science Foundation of China [grant number 52278424]; the Innovation Program for Automobile Environmental Protection by FAW-Volkswagen & China Environmental Protection Foundation; the Key Laboratory of Road and Traffic Engineering of the Ministry of Education, Tongji University; and Young Elite Scientist Sponsorship Program by China Association for Science and Technology [YESS20230576].

## Reference

Arrigo, R., Sasaki, T., Callison, J., Gianolio, D., Schuster, M.E., 2022. Monitoring Dynamics of Defects and Single Fe Atoms in N-functionalized Few-layer Graphene by in Situ Temperature Programmed Scanning Transmission Electron Microscopy. J. Energy Chem. 71, 657-657. https://doi.org/10.1016/j.jechem.2021.08.003

Bi, H., Shang, W.L., Chen, Y., Wang, K., 2022. Joint Optimization for Pedestrian, Information and Energy Flows in Emergency Response Systems with Energy Harvesting and Energy Sharing. IEEE T. Intell. Transp. 23(11), 22421-35. https://doi.org/10.1109/TITS.2022.3159503

Bi, H., Shang, W.L., Chen, Y., Wang, K., Yu, Q., Sui, Y., 2021. GIS Aided Sustainable Urban Road

Management with A Unifying Queueing and Neural Network Model. Appl. Energy. 291, 116818. https://doi.org/10.1016/j.apenergy.2021.116818

Birčáková, Z., Onderko, F., Dobák, S., Kollár, P., Füzer, J., Bureš, R., et al., 2022. Eco-friendly Soft Magnetic Composites of Iron Coated by Sintered Ferrite via Mechanofusion. J. Magn. Magn. Mater. 543, 168627. https://doi.org/10.1016/j.jmmm.2021.168627

Ceravolo, R., Miraglia, G., Surace, C., 2017. Fatigue Damage Assessment of Electric Roads Based on Probabilistic Load Models. J. Phys.: Conf. 842, 012037. https://doi.org/10.1088/1742-6596/842/1/012037

Ceravolo, R., Miraglia, G., Surace, C., Zanotti Fragonara, L., 2016. A Computational Methodology for Assessing the Time-Dependent Structural Performance of Electric Road Infrastructures. Computer-Aided Civil and Infrastructure Engineering. 31(9), 701-16. https://doi.org/10.1111/mice.12199

Chen, F., Kringos, N., 2014. Towards New Infrastructure Materials for On-the-road Charging: A Study of Potential Materials, Construction and Maintenance. IEEE IEVC, Florence, Italy.

Chen, Y., Wu, J., Zhang, H., Guo, L., Lu, F., Jin, N., et al, 2023. A Parameter Tuning Method for a Double-Sided LCC Compensated IPT System with Constant-Voltage Output and Efficiency Optimization. IEEE Transactions on Power Electronics. 38(3), 4124-39. https://doi.org/10.1109/TPEL.2022.3218709

Crabtree, G., 2019. The Coming Electric Vehicle Transformation. Science. 366(6464), 422-424. https://doi.org/10.1126/science.aax0704

Edwards, K.A.T., Al-Abed, S.H., Hosseini, S., Brake, N.A., 2019. Properties of A Magnetic Concrete Core Transformer for Application in Wireless Power Transfer Systems. Constr. Build. Mater. 227, 117041. https://doi.org/10.1016/j.conbuildmat.2019.117041

Gao, W., Dong, Y., Ma, Y., Wu, H., Jia, X., Liu, Z., et al., 2023. Effects of Structural Transformation on Magnetic Properties of AlCoFeCr High-entropy Soft Magnetic Powder Cores by Adjusting Co/Fe Ratio. Mater. Des. 225, 111537. https://doi.org/10.1016/j.matdes.2022.111537

GB/T 17671-2021, 2021. Method of Testing Cements - Determination of Strength. (Standard in China).

GB/T 3848-2017, 2017. Hardmetals - Determination of (The Magnetization) Coercivity. (Standard in China).

GB/T 38775.3-2020, 2020. Electric vehicle wireless power transfer - Part 3: Specific requirements. (Standard in China).

Gu, G., Chen, F., Ma, T., Xu, F., Yang, D., 2022a. Electromagnetic and Mechanical Properties of Soft Magnetic

Cement Composite for Airport Runway Induction Heating: Experimental and Simulation Analyses. J. Clean Prod. 332, 130141. https://doi.org/10.1016/j.jclepro.2021.130141

Gu, G., Ma, T., Chen, F., Li, H., Pei, Y., Xu, F., 2023. Soft Magnetic Geopolymer in Airport Pavement Induction Heating: Effect of Fe Powder Distribution on the Electromagnetic Loss. Ceram. Int. 49(2), 1720-1730. https://doi.org/10.1016/j.ceramint.2022.09.136

Gu, G., Ma, T., Chen, F., Xu, F., Zhang, J., 2022b. Electromagnetic and Mechanical Properties of FA-GBFS Geopolymer Composite Used for Induction Heating of Airport Pavement. Cem. Concr. Compos. 129, 104503. https://doi.org/10.1016/j.cemconcomp.2022.104503

Guo, L., Wang, H., 2022. A Novel Design of Partially Magnetized Pavement for Wireless Power Transfer to Electric Vehicles with Improved Efficiency and Cost Saving. Energy Convers. Manage. 252, 115080. https://doi.org/10.1016/j.enconman.2021.115080.

Hu, Y., Wang, Z., Li, X., 2020. Impact of Policies on Electric Vehicle Diffusion: An Evolutionary Game of Small World Network Analysis. J. Clean Prod. 265, 121703. https://doi.org/10.1016/j.jclepro.2020.121703

Ji, Z.Y., Wang, Q., Wang, Z.H., Duan, Y.P., Dong, C., Liaw, P.K., 2022. Electromagnetic Wave-Absorbing Behavior of Soft-magnetic Medium Entropy Alloys with BCC/$L2_1$ Coherent Microstructure. Mater. Des. 222, 111054. https://doi.org/10.1016/j.matdes.2022.111054

Kim, H., Song, C., Kim, D.H., Jung, D.H., Kim, I.M., Kim, Y.I., et al., 2016. Coil Design and Measurements of Automotive Magnetic Resonant Wireless Charging System for High-Efficiency and Low Magnetic Field Leakage. IEEE Trans. Microwave Theory Tech. 64(2), 383-400, https://doi.org/10.1109/TMTT.2015.2513394

Kim, Y., Yuk, H., Zhao, R., Chester, S.A., Zhao, X., 2018. Printing Ferromagnetic Domains for Untethered Fast-transforming Soft Materials. Nature. 558(7709), 274-279. https://doi.org/10.1038/s41586-018-0185-0

Lal, A., You, F., 2023. Will Reshoring Manufacturing of Advanced Electric Vehicle Battery Support Renewable Energy Transition and Climate Targets? Science. 9(24), 6740. https://doi.org/10.1126/sciadv.adg6740

Li, F., Li, Y., Zhou, S., Chen, Y., Sun, X., Deng, Y., 2022. Wireless Power Transfer Tuning Model of Electric Vehicles with Pavement Materials as Transmission Media for energy conservation. Appl. Energy. 323, 119631. https://doi.org/10.1016/j.apenergy.2022.119631

Li, F., Sun, X., Zhou, S.Q., Chen, Y.H., Hao, Z.B., Yang, Z.N., 2021. Infrastructure Material Magnetization Impact Assessment of Wireless Power Transfer Pavement Based on Resonant Inductive Coupling. IEEE T. Intell. Transp, 23(11), 22400-8. https://doi.org/10.1109/TITS.2021.3099490

Li, X., Peng, J., Duan, L., Wang, W., Li, W., 2024. Effect of Sol-type Nano-SiO2 and Plasticizer on the Properties of Fly Ash-Slag Geopolymer. Journal of Municipal Technology, 42(2): 21-27. http://dx.doi.org/10.19922/j.1009-7767.2024.02.021

Limb, B.J., Asher, Z.D., Bradley, T.H., Sproul, E., Quinn, J.C., 2018. Economic Viability and Environmental Impact of In-Motion Wireless Power Transfer. IEEE T. Transp. Electr. 5(1), 134-46, https://doi.org/10.1109/TTE.2018.2876067

Liu, F., Yang, Y., Jiang, D., Ruan, X., Chen, X., 2017. Modeling and Optimization of Magnetically Coupled Resonant Wireless Power Transfer System with Varying Spatial Scales. IEEE Transactions on Power Electronics. 32(4), 3240-50. https://doi.org/10.1109/TPEL.2016.2581840

Liu, K., Fu, C., Wang, H., Wang, F., Xu, P., Kan, C., 2020a. Exploring the Energy-Saving Potential of Electromagnetic Induction Pavement via Magnetic Concentrating Technique. Energy. 211, 118650. https://doi.org/10.1016/j.energy.2020.118650

Liu, K., Xu, P., Wang, F., Jin, C., Huang, M., Dai, D., et al., 2020b. Deicing Efficiency Analysis and Economic-Environment Assessment of A Novel Induction Heating Asphalt Pavement. J. Clean Prod. 273, 123123. https://doi.org/10.1016/j.jclepro.2020.123123

Liu, L., Yue, Q., Li, G.Q., Xu, K., Wang, J., Wu, Z.Y., et al., 2019. Influence of SiO2 Insulation Layers Thickness Distribution on Magnetic Behaviors of Fe-Si@SiO2 Soft Magnetic Composites. J. Phys. Chem. Solids. 132, 76-82. https://doi.org/10.1016/j.jpcs.2019.04.016

Lu, D., Jiang, X., Leng, Z., Zhang, S., Wang, D., Zhong, J., 2023a. Dual Responsive Microwave Heating-Healing System in Asphalt Concrete Incorporating Coal Gangue and Functional Aggregate. J. Clean Prod. 422. http://dx.doi.org/10.1016/j.jclepro.2023.138648

Lu, D., Leng, Z., Lu, G.Y., Wang, D.Y., Huo, Y.L., 2023b. A Critical Review of Carbon Materials Engineered Electrically Conductive Cement Concrete and Its Potential Applications. Int. J. Smart Nano Mater. 14(2), 189-215. http://dx.doi.org/10.1080/19475411.2023.2199703

Lu, D., Jiang, X., Leng, Z., 2024a. Sustainable Microwave-Heating Healing Asphalt Concrete Fabricated with

Waste Microwave-Sensitive Fillers. J. Clean Prod. 434, 140343. https://doi.org/10.1016/j.jclepro.2023.140343

Lu, D., Jiang, X., Qu, F., Huo, Y., 2024b. Mitigating Sulfate Ions Migration in Concrete: A Targeted Approach to Address Recycled Concrete Aggregate's Impact. J. Clean Prod. 442, 141135. http://dx.doi.org/10.1016/j.jclepro.2024.141135

Ma, T., Gu, G., Chen, F., Wang, N., 2023. Influence of Iron Powder Content on The Electromagnetic And Mechanical Performance of Soft Magnetic Geopolymer Composite. Journal of Road Engineering. https://doi.org/10.1016/j.jreng.2023.05.002

Mahmud, M.H., Elmahmoud, W., Barzegaran, M.R., Brake, N., 2017. Efficient Wireless Power Charging of Electric Vehicle by Modifying the Magnetic Characteristics of the Transmitting Medium. IEEE Trans. Magn. 53(6), 9100205. https://doi.org/10.1109/TMAG.2017.2654164

Meng, X., Zhang, S., Xu, W., Pi, Z., Li, H., Xu, M., 2024. Mechanical Performance and Solidification Mechanism of Fluidized Solidified Soil of Slag Calcium Sulfoaluminate Cement. Journal of Municipal Technology. 42(2): 14-20. https://doi.org/10.19922/j.1009-7767.2024.02.014

Onar, O.C., Miller, J.M., Campbell, S.L., Coomer, C., White, C.P., Seiber, L.E., 2013. Oak Ridge National Laboratory Wireless Power Transfer Development for Sustainable Campus Initiative. IEEE ITEC, 1-8, Detroit, MI, USA. https://doi.org/10.1109/ITEC.2013.6574506

Pei, Y., Le Bihan, Y., Bensetti, M., Pichon, L., 2021. Comparison of Coupling Coils for Static Inductive Power-Transfer Systems Taking into Account Sources of Uncertainty. Sustainability. 13(11), 6324. https://doi.org/10.3390/su13116324.

Rasekh, N., Dabiri, S., Rasekh, N., Mirsalim, M., Bahiraei, M., 2020. Thermal Analysis and Electromagnetic Characteristics of Three Single-Sided Flux Pads for Wireless Power Transfer. J. Clean Prod. 243, 118561. https://doi.org/10.1016/j.jclepro.2019.118561

Rubino, L., Capasso, C., Veneri, O., 2017. Review on Plug-in Electric Vehicle Charging Architectures Integrated with Distributed Energy Sources for Sustainable Mobility. Appl. Energy. 207, 438-64. https://doi.org/10.1016/j.apenergy.2017.06.097

Sadhukhan, M., Deb, B.M., 2021. Structure, Dynamics and Quantum Chaos in Atoms and Molecules under Strong Magnetic Fields. J. Indian Chem. Soc. 98(9), 100112. https://doi.org/10.1016/j.jics.2021.100112

Schubert, D.W., Werner, S., Hahn, I., Solovieva, V., 2019. Effect of Particle Size and Size Distribution on The

Permeability of Soft Magnetic Liquid Silicone Rubber Composites. Compos. Sci. Technol. 177, 26-33. https://doi.org/10.1016/j.compscitech.2019.04.005

Shang, W.L., Gao, Z., Daina, N., Zhang, H., Long, Y., Guo, Z., et al., 2022. Benchmark Analysis for Robustness of Multi-Scale Urban Road Networks Under Global Disruptions. IEEE T. Intell. Transp. https://doi.org/10.1109/TITS.2022.3149969

Shang, W.L., Chen, J., Bi, H., Sui, Y., Chen, Y., Yu, H., 2021. Impacts of COVID-19 Pandemic on User Behaviors and Environmental Benefits of Bike Sharing: A Big-Data Analysis. Appl. Energy 285, 116429. https://doi.org/10.1016/j.apenergy.2020.116429

Talluri, G., Bindi, M., Luchetta, A., Grasso, F., Luchetti, L., Paolucci, L., 2021. Analysis of Power Losses Due to Magnetic Shielding for Electric Vehicle Wireless Charging. IEEE 15th International Conference on CPE-POWERENG, 1-6. https://doi.org/10.1109/CPE-POWERENG50821.2021.9501223

Tavakoli, R., Echols, A., Pratik, U., Pantic, Z., Pozo, F., Malakooti, A., et al., 2017. Magnetizable Concrete Composite Materials for Road-Embedded Wireless Power Transfer Pads. IEEE ECCE, 4041-8.

Thomas, S., 2023. Connecting with Wireless Power Transfer. Nature Electronics. 6(2), 106. https://doi.org/10.1038/s41928-023-00933-z

Thorsson, L., Unosson, M., Teresa P.M., Jin, X., Tiberto, P., Barrera, G., et al., 2022. Selective Laser Melting of A Fe-Si-Cr-B-C-based Complex-Shaped Amorphous Soft-Magnetic Electric Motor Rotor with Record Dimensions. Mater. Des. 215, 110483. https://doi.org/10.1016/j.matdes.2022.110483

Trompetter, B., Leveneur, J., Max, G.W., Rumsey, B., Turner, J., Weir, G., et al., 2023. Ferrite Based Soft Magnetic Composite Development Intended for Inroad Charging Application. J. Magn. Magn. Mater. 570, 170530. https://doi.org/10.1016/j.jmmm.2023.170530

Varga, L.K., Gercsi, Z., Kovács, G., Mazaleyrat, F., 2006. The Influence of Size on Coercive Field of Ultra Soft Magnetic Materials. J. Magn. Magn. Mater. 301(2), 527-31. https://doi.org/10.1016/j.jmmm.2005.08.004

Wang, Q., Wu, Z., Huang, J., Du, Z., Yue, Y., Chen, D., et al., 2021. Integration of Sensing and Shape-Deforming Capabilities for A Bioinspired Soft Robot. Composites, Part B. 223, 109116. https://doi.org/10.1016/j.compositesb.2021.109116

Yang, S., Yan, X., He, H., Yang, P., Peng, Z., Cui, H., 2018. Control Strategy for Vehicle Inductive Wireless Charging Based on Load Adaptive and Frequency Adjustment. Energies 11(5), 1222.

https://doi.org/10.3390/en11051222

Zhang, J., Gao, L., Dong, Z., 2023. Review on Materials and Technology of Multifunctional Maintenance of Asphalt Pavement. Journal of Municipal Technology. 41(10): 80-91. https://doi.org/10.19922/j.1009-7767.2023.10.080

Zhang, Y., Liu, C., Zhou, M., Mao, X., 2023. A Novel Asymmetrical Quadrupolar Coil for Interoperability of Unipolar, Bipolar, and Quadrupolar Coils in Electric Vehicle Wireless Charging Systems. IEEE Transactions on Industrial Electronics, 71(4), 4300-03. https://doi.org/10.1109/TIE.2023.3277123

Zhou, J., Wang, Q., Hui, X., Zeng, Q., Xiong, Y., Yin, K., et al., 2020. A Novel FeNi-Based Bulk Metallic Glass with High Notch Toughness Vver 70 MPa $m^{1/2}$ Combined with Excellent Soft Magnetic Properties. Mater. Des. 191, 108597. https://doi.org/10.1016/j.matdes.2020.108597

2023. Interim Regulations on the Radio Management of Wireless Charging (Power Transmission) Equipment. (Standard in China).